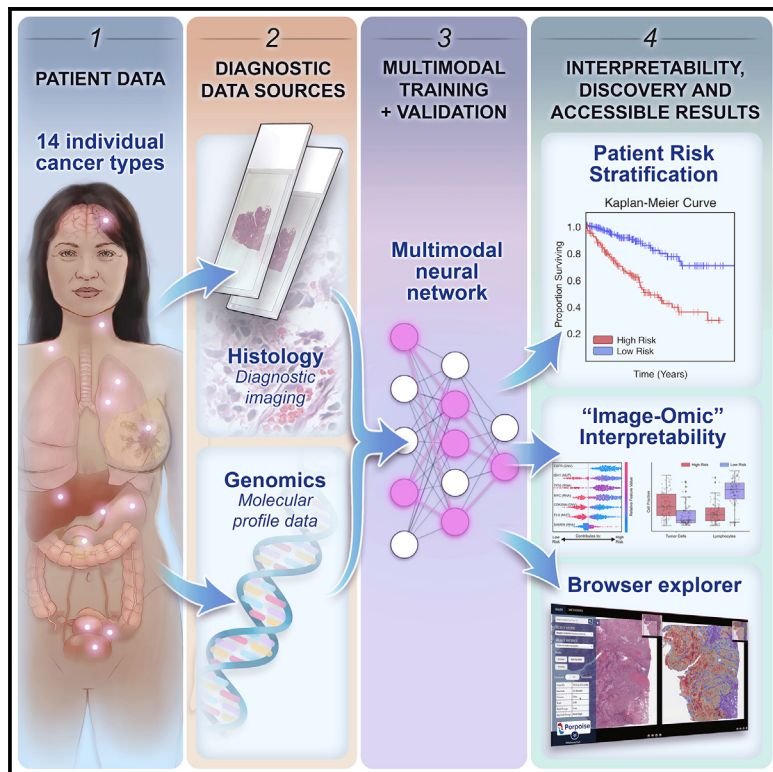


Pan-cancer integrative histology-genomic analysis via multimodal deep learning

Graphical abstract



Authors

Richard J. Chen, Ming Y. Lu,
Drew F.K. Williamson, ...,
Mane Williams, Bumjin Joo,
Faisal Mahmood

Correspondence

faisalmahmood@bwh.harvard.edu

In brief

Chen et al. present a pan-cancer analysis that uses deep learning to integrate whole-slide pathology images and molecular features to predict cancer prognosis, with multimodal interpretability used to elucidate morphologic and molecular correlates of prognosis.

Highlights

- Multimodal data fusion improves prognostic models for a majority of cancer types
- Multimodal attribution elucidates the importance of individual modalities
- Model interpretability elucidates morphologic and molecular correlates of prognosis

Article

Pan-cancer integrative histology-genomic analysis via multimodal deep learning

Richard J. Chen,^{1,2,3,4,5} Ming Y. Lu,^{1,2,4,5,6,8} Drew F.K. Williamson,^{1,2,4,5,8} Tiffany Y. Chen,^{1,4,5,8} Jana Lipkova,^{1,4,5} Zahra Noor,¹ Muhammad Shaban,^{1,2,4,5} Maha Shady,^{1,3,4,5} Mane Williams,^{1,2,3,4,5} Bumjin Joo,¹ and Faisal Mahmood^{1,2,4,5,7,9,*}

¹Department of Pathology, Brigham and Women's Hospital, Harvard Medical School, Boston, MA, USA

²Department of Pathology, Mass General Hospital, Harvard Medical School, Boston, MA, USA

³Department of Biomedical Informatics, Harvard Medical School, Boston, MA, USA

⁴Cancer Program, Broad Institute of Harvard and MIT, Cambridge, MA, USA

⁵Cancer Data Science Program, Dana-Farber/Harvard Cancer Institute, Boston, MA, USA

⁶Department of Electrical Engineering and Computer Science, MIT, Cambridge, MA, USA

⁷Harvard Data Sciences Initiative, Harvard University, Cambridge, MA, USA

⁸These authors contributed equally

⁹Lead contact

*Correspondence: faisalmahmood@bwh.harvard.edu

<https://doi.org/10.1016/j.ccell.2022.07.004>

SUMMARY

The rapidly emerging field of computational pathology has demonstrated promise in developing objective prognostic models from histology images. However, most prognostic models are either based on histology or genomics alone and do not address how these data sources can be integrated to develop joint image-omic prognostic models. Additionally, identifying explainable morphological and molecular descriptors from these models that govern such prognosis is of interest. We use multimodal deep learning to jointly examine pathology whole-slide images and molecular profile data from 14 cancer types. Our weakly supervised, multimodal deep-learning algorithm is able to fuse these heterogeneous modalities to predict outcomes and discover prognostic features that correlate with poor and favorable outcomes. We present all analyses for morphological and molecular correlates of patient prognosis across the 14 cancer types at both a disease and a patient level in an interactive open-access database to allow for further exploration, biomarker discovery, and feature assessment.

INTRODUCTION

Cancer is defined by hallmark histopathological, genomic, and transcriptomic heterogeneity in the tumor and tissue microenvironment that contributes toward variability in treatment response rates and patient outcomes (Marusyk et al., 2012). The current clinical paradigm for many cancer types involves the manual assessment of histopathologic features such as tumor invasion, anaplasia, necrosis, and mitoses, which are then used as grading and staging criteria for stratifying patients into distinct risk groups for therapeutic decision-making. For instance, in the tumor, nodes, and metastases (TNM) staging system, primary tumors are categorized into stages based on tumor severity (e.g., size, growth, atypia), which are then used in treatment planning, eligibility for surgical operations, radiation dosage, and other treatment decisions (Amin et al., 2017). However, the subjective interpretation of histopathologic features has been demonstrated to suffer from large inter- and intra-observer variability, and patients in the same grade or stage still have significant variability in outcomes. While many histopathologic biomarkers have been established for diagnostic tasks, most are based on the morphology and location of tumor cells

alone and lack a fine-grained understanding of how the spatial organization of stromal, tumor, and immune cells in the broader tumor microenvironment contributes toward patient risk (Marusyk et al., 2012; Chang et al., 2013; Heindl et al., 2015; Kather et al., 2018; Tarantino et al., 2021).

Recent advancements made in deep learning for computational pathology have enabled the use of whole-slide images (WSIs) for automated cancer diagnosis and quantification of morphologic phenotypes in the tumor microenvironment. Using weakly supervised learning, slide-level clinical annotations can be used to guide deep-learning algorithms in recapitulating routine diagnostic tasks such as cancer detection, grading, and subtyping (Campanella et al., 2019; Lu et al., 2021). Though such algorithms can reach performance on par with human experts for narrowly defined problems, the quantification of novel prognostic morphological features is limited, as training with subjective human annotations may fail to extract heretofore unrecognized properties that could be used to improve patient prognostication (Echle et al., 2021). To capture more objective and prognostic morphological features not extracted in routine clinical workflows, recent deep-learning-based approaches propose supervision using outcome-based labels such as



disease-free and overall survival times as ground truth (Harder et al., 2019; Courtiol et al., 2019; Kather et al., 2019a, 2019b; Kulikarni et al., 2020; Wuclyzyn et al., 2020, 2021). Indeed, recent work has shown there is enormous potential in using deep learning for automated biomarker discovery of novel and prognostic morphological determinants (Beck et al., 2011; Echle et al., 2021; Diao et al., 2021).

Though prognostic morphological biomarkers may potentially be elucidated using outcome-based labels as supervision in WSIs, in the broader context, cancer prognostication is a multimodal problem that is driven by markers in histology, clinical data, and genomics (Ludwig and Weinstein, 2005; Gentzler et al., 2014; Fridman et al., 2017; Mobadersany et al., 2018; Cheerla and Gevaert, 2019; Vale-Silva, and Rohr, 2021). From the emergence of next-generation sequencing and development of targeted molecular therapies, therapeutic decision-making processes for many cancer types have become increasingly complex due to the inclusion of molecular biomarkers in prognostication (Hyman et al., 2015). For instance, the presence of epidermal growth factor receptor (*EGFR*) exon 19 deletions and exon 21 p.Leu858Arg substitutions are indications for the use of targeted therapies such as erlotinib in *EGFR* mutant lung and pancreatic cancers (Mayekar and Bivona, 2017; Zhou et al., 2021). In combination with histological assessment, joint image-omic biomarkers such as oligodendrogloma and astrocytoma histologies with *IDH1* mutation and 1p/19q-codeletion status is able to perform fine-grained stratification of patients into low-, intermediate-, and high-risk groups (Louis et al., 2016; Bai et al., 2016; Cloughesy et al., 2019), and determining the presence or absence of these integrated biomarkers has become standard of care in assessment of brain tumors by pathologists. Using deep learning, multimodal fusion of molecular biomarkers and extracted morphological features from WSIs has potential clinical application in not only improving precision in patient risk stratification but could also assist in the discovery and validation of multimodal biomarkers where combinatory effects of histology and genomic biomarkers are not known (Bera et al., 2019). Recent multimodal studies performed on the TCGA have focused on learning genotype-phenotype associations via predicting molecular aberrations using histology, which can assist in deciding targeted molecular therapies for patients without next-generation sequencing (Coudray et al., 2018; Kather et al., 2019a, 2019b, 2020; Fu et al., 2020).

RESULTS

Deep-learning-based multimodal integration

In order to address the challenges in developing joint image-omic biomarkers that can be used for cancer prognosis, we propose a deep-learning-based multimodal fusion (MMF) algorithm that uses both H&E WSIs and molecular profile features (mutation status, copy-number variation, RNA sequencing [RNA-seq] expression) to measure and explain relative risk of cancer death (Figure 1A). Our multimodal network is capable of not only integrating these two modalities in weakly supervised learning tasks such as survival-outcome prediction but also explaining how histopathology features, molecular features, and their interactions correlate with low- and high-risk patients (Figures 1B–1E). After risk assessment within a patient

cohort, our network uses both attention- and attribution-based interpretability as an untargeted approach for estimating prognostic markers across all patients (Figures 1B–1F). Our study uses 6,592 gigapixel WSIs from 5,720 patient samples across 14 cancer types from the TCGA (Table S1). For each cancer type, we trained our multimodal model in a 5-fold cross-validation using our weakly supervised paradigm and conducted ablation analyses comparing the performance between unimodal and multimodal prognostic models. Following training and model evaluation, we conducted extensive analyses on the interpretability of our networks, investigating local- and global-level image-omic explanations for each cancer type, quantifying the tissue microarchitecture corresponding relevant morphology, and also investigating shifts in feature importance when comparing unimodal interpretability versus multimodal interpretability.

We additionally developed a research tool that uses model explanations of both WSIs and molecular profile data to drive the discovery of new prognostic biomarkers. Using our multimodal network, we developed the Pathology-Omics Research Platform for Integrative Survival Estimation (PORPOISE), an interactive platform that directly yields prognostic markers learned by our model for thousands of patients across multiple cancer types, available at <http://pancancer.mahmoodlab.org> (interactive demo). Specifically, PORPOISE allows the user to visualize (1) raw H&E image pyramidal TIFFs overlayed with attention-based interpretability from both unimodal and multimodal training, (2) local explanations of molecular features using attribution-based interpretability for each patient, and (3) global patterns of morphological and molecular feature importance for each disease model. To validate that PORPOISE can be used to drive the discovery of human-identifiable prognostic biomarkers, we analyzed high-attention morphological regions in WSIs and further quantified the tumor microenvironment to quantify morphologic correlates of high- and low-risk patients.

Multimodal integration improves patient risk stratification

We first evaluated our proposed MMF deep-learning model using 5-fold cross-validation on the paired WSI-molecular datasets from 14 cancer types. We also compared our model with unimodal deep-learning models trained with one modality: an attention-based multiple-instance learning (AMIL) model that uses only WSIs and a self-normalizing network (SNN) model that uses only molecular features. To compare the performances of these models, we used a cross-validated concordance index (c-Index) to measure the predictive performance of each model, Kaplan-Meier curves to visualize the quality of patient stratification between predicted low- and high-risk patient populations, and the log rank test to assess patient stratification statistical significance in distinguishing low- and high-risk groups at the 50% percentile of predicted risk scores (Figure 2A, 2B, and S1; Table S2). In addition to the c-Index, we also report dynamic area under the curve (AUC; termed survival AUC), which corrects for optimistic bias from censorship in computing model performance (Table S3).

Across the 14 cancer types, MMF achieved an overall c-Index of 0.644, whereas AMIL and SNN had overall c-Indices of 0.578

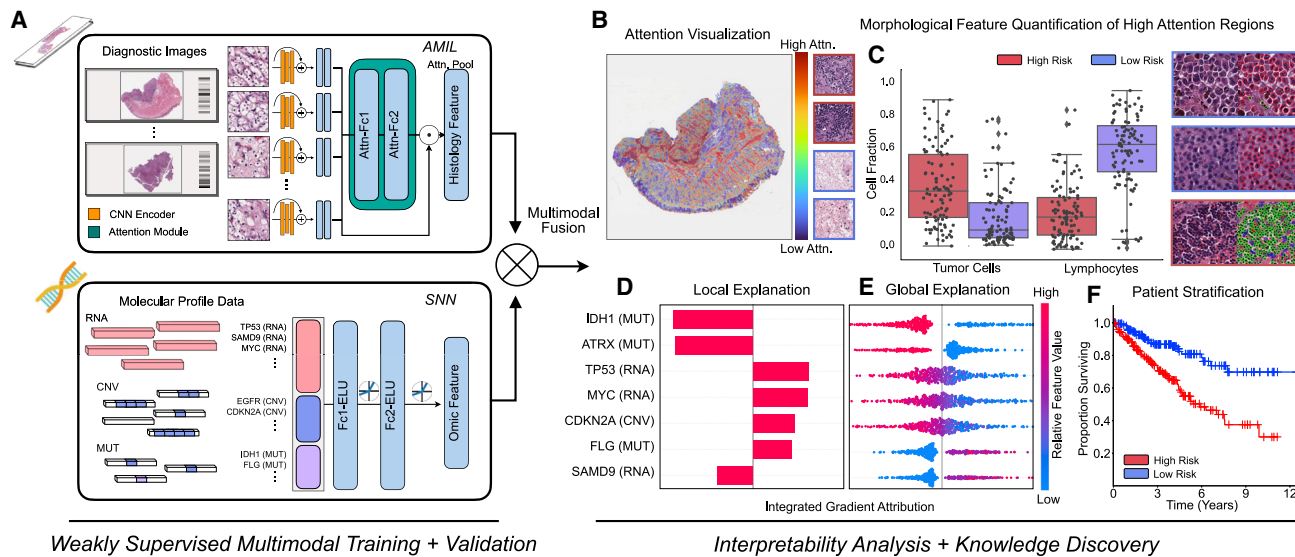


Figure 1. Pathology-Omic Research Platform for Integrative Survival Estimation (PORPOISE) workflow

(A) Patient data in the form of digitized high-resolution formalin-fixed paraffin-embedded (FFPE) H&E histology glass slides (known as WSIs) with corresponding molecular data are used as input in our algorithm. Our multimodal algorithm consists of three neural network modules together: (1) an attention-based multiple-instance learning (AMIL) network for processing WSIs, (2) a self-normalizing network (SNN) for processing molecular data features, and (3) a multimodal fusion layer that computes the Kronecker Product to model pairwise feature interactions between histology and molecular features.

(B) For WSIs, per-patient local explanations are visualized as high-resolution attention heatmaps using attention-based interpretability, in which high-attention regions (red) in the heatmap correspond to morphological features that contribute to the model's predicted risk score.

(C) Global morphological patterns are extracted via cell quantification of high-attention regions in low- and high-risk patient cohorts.

(D) For molecular features, per-patient local explanations are visualized using attribution-based interpretability in integrated gradients.

(E) Global interpretability for molecular features is performed via analyzing the directionality, feature value, and magnitude of gene attributions across all patients.

(F) Kaplan-Meier analysis is performed to visualize patient stratification of low- and high-risk patients for individual cancer types.

See also Table S1.

and 0.606, respectively. On survival AUC, similar improvement in multimodal integration was found with an overall performance of 0.662 compared with 0.615 and 0.588 in SNN and AMIL, respectively (Table S2). In one-versus-all model performance comparisons on individual cancer types, MMF achieved the highest c-Index on 12 out of 14 (12/14) cancer types, with models for 10/14 cancer types demonstrating statistical significance in binary patient stratification (Figures 2A–2C). Compared with SNN, which uses only molecular features, MMF also demonstrated consistent performance in both c-Index and survival AUC across all cancer types. Though SNN had comparable performance on some cancer types, we observed both substantial improvement in model performance and patient stratification for breast cancer (BRCA), colorectal adenocarcinoma (COADREAD), lung adenocarcinoma (LUAD), pancreatic adenocarcinoma (PAAD), and uterine corpus endometrial carcinoma (UCEC), which did not show significance in SNN patient stratification (Figure 2B; Table S2). Compared with AMIL, MMF showed improvement on all cancer types except lung squamous cell carcinoma (LUSC) and UCEC, with improvement in patient stratification significance in 7/14 cancer types. We note that skin cutaneous melanoma (SKCM) has an admixture of easily distinguished disease forms (e.g., containing both primary and metastatic cases), which may optimistically bias model performances. Overall, however, model performances were found to improve following multimodal integration for almost all cancer types (Figure 2B). In examining unimodal models that were close

to MMF performance, SNN showed significance in stratifying clear cell renal cell carcinoma (KIRC) and papillary renal cell carcinoma (KIRP) (though predicted risk groups are better delineated in MMF), and AMIL showed significance in stratifying liver hepatocellular carcinoma (LIHC), stomach adenocarcinoma (STAD), and UCEC.

Among all single cancer types included in our study, KIRP had the largest performance increase with multimodal training, reaching a c-Index performance of 0.816 (95% confidence interval [CI]: 0.705–0.880, $p = 3.83 \times 10^{-4}$, log rank test), compared with 0.539 (95% CI: 0.408–0.625, $p = 5.86 \times 10^{-1}$, log rank test) using AMIL and 0.779 (95% CI: 0.678–0.857, $p = 2.27 \times 10^{-3}$, log rank test) using SNN (Table S2). Following the correction of potential optimistic bias with high censorship via survival AUC evaluation, we observed similar model performances with MMF reaching an AUC of 0.791 (SD: 0.102) compared with 0.530 (SD: 0.082) in AMIL and 0.743 (SD: 0.095). PAAD demonstrated substantial improvement with multimodal training, with a c-Index of 0.653 (95% CI: 0.571–0.696, $p = 1.69 \times 10^{-3}$, log rank test), compared with 0.580 (95% CI: 0.485–0.613, $p = 2.30 \times 10^{-1}$, log rank test) using AMIL and 0.593 (95% CI: 0.507–0.656, $p = 5.59 \times 10^{-2}$, log rank test) using SNN (Table S2). For PAAD, we observed that training unimodal models using either only histology or genomics did not show statistical significance, as Kaplan-Meier survival curves demonstrate poor stratification of predicted low- and high-risk groups of patients with low survival in these two cancer types. However, these groups were

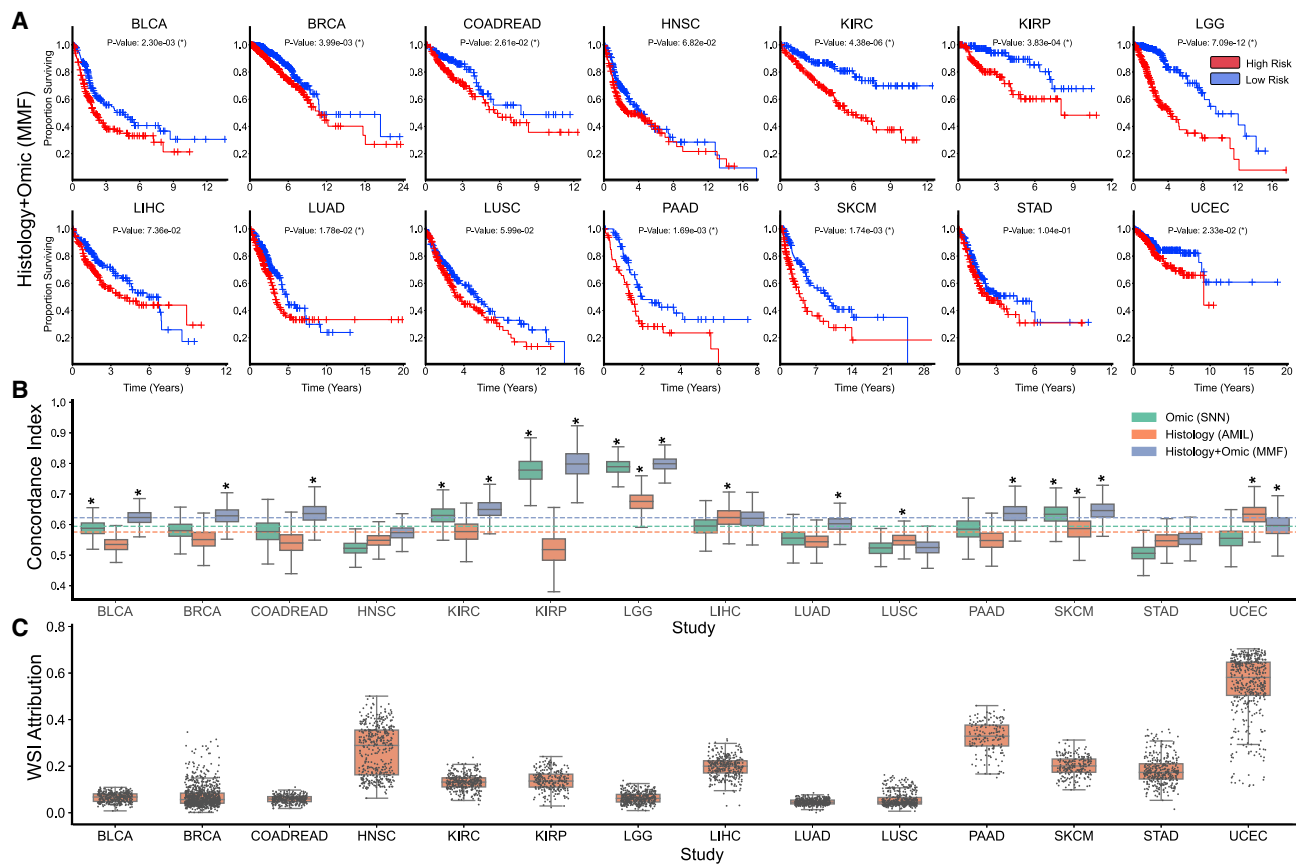


Figure 2. Model performances of PORPOISE and understanding impact of multimodal training

(A) Kaplan-Meier analysis of patient stratification of low- and high-risk patients via MMF across all 14 cancer types. Low and high risks are defined by the median 50% percentile of hazard predictions via MMF. Log rank test was used to test for statistical significance in survival distributions between low- and high-risk patients (* $p < 0.05$).

(B) c-Index performance of SNN, AMIL, and MMF in each cancer type in a 5-fold cross-validation ($n = 5,720$). Horizontal line for each model shows average c-Index performance across all cancer types. Boxplots correspond to c-Indices of 1,000 bootstrap replicates on the aggregated risk predictions.

(C) Distribution of WSI attribution across 14 cancer types. Each dot represents the proportion of feature attribution given to the WSI modality input compared with molecular feature input. Attributions were computed on the aggregated risk predictions in each disease model. Boxes indicate quartile values and whiskers extend to data points within 1.5× the interquartile range.

See also Figures S1–S3, S11, S12 and Tables S1, S2, and S3.

disentangled following multimodal integration, which is in line with our observed improvement in MMF performance in PAAD. We demonstrate similar stratification results in BRCA, COADREAD, and LUAD in separating low-survival groups using MMF (Figures S2, S3, S6, and S11).

In addition to conducting ablation studies in comparing unimodal and multimodal models, we also assessed Cox proportional hazard models using age, gender, and tumor grade covariates as baselines, which were still outperformed by MMF (Table S3). In head-to-head comparisons on cancer types with only available grade information, AMIL outperforms Cox models with an average c-Index of 0.601 compared with 0.582, which suggests that current subjective assessments for tumor grade in cancer prognosis may be refined using objective, deep-learning-based phenotyping for evaluating prognosis.

We additionally quantify the prognostic importance of each modality, giving us the ability to determine which cancer types warrant development of multimodal prognostic models and for

which tumor type histology or genomics alone may be enough to build sufficient prognostic models. In quantifying the contribution of using WSIs in cancer prognosis, WSIs on average accounted for 16.8% of input attributions in MMF for all cancer types, which suggests that molecular features drive most of the risk prediction in MMF (Figure 2C; Table S3). This substantiates the observation that molecular profiles are more prognostic for survival than WSIs in most cancer types (in comparing the performances of SNN and AMIL). However, we note that for MMF models evaluated on UCEC, WSIs contributed to 55.1% of all input attributions, which corroborates with high AMIL performance on this cancer type. We also observe relatively larger average WSI contributions in head neck squamous cell carcinoma (HNSC), STAD, and LIHC as well, which corroborates with the cancer types in which AMIL outperformed SNN. For LUSC, in which AMIL also outperformed SNN, we observe a relatively low average WSI attribution of 5.8%, which potentially corroborates MMF under-performance, as the model was unable to

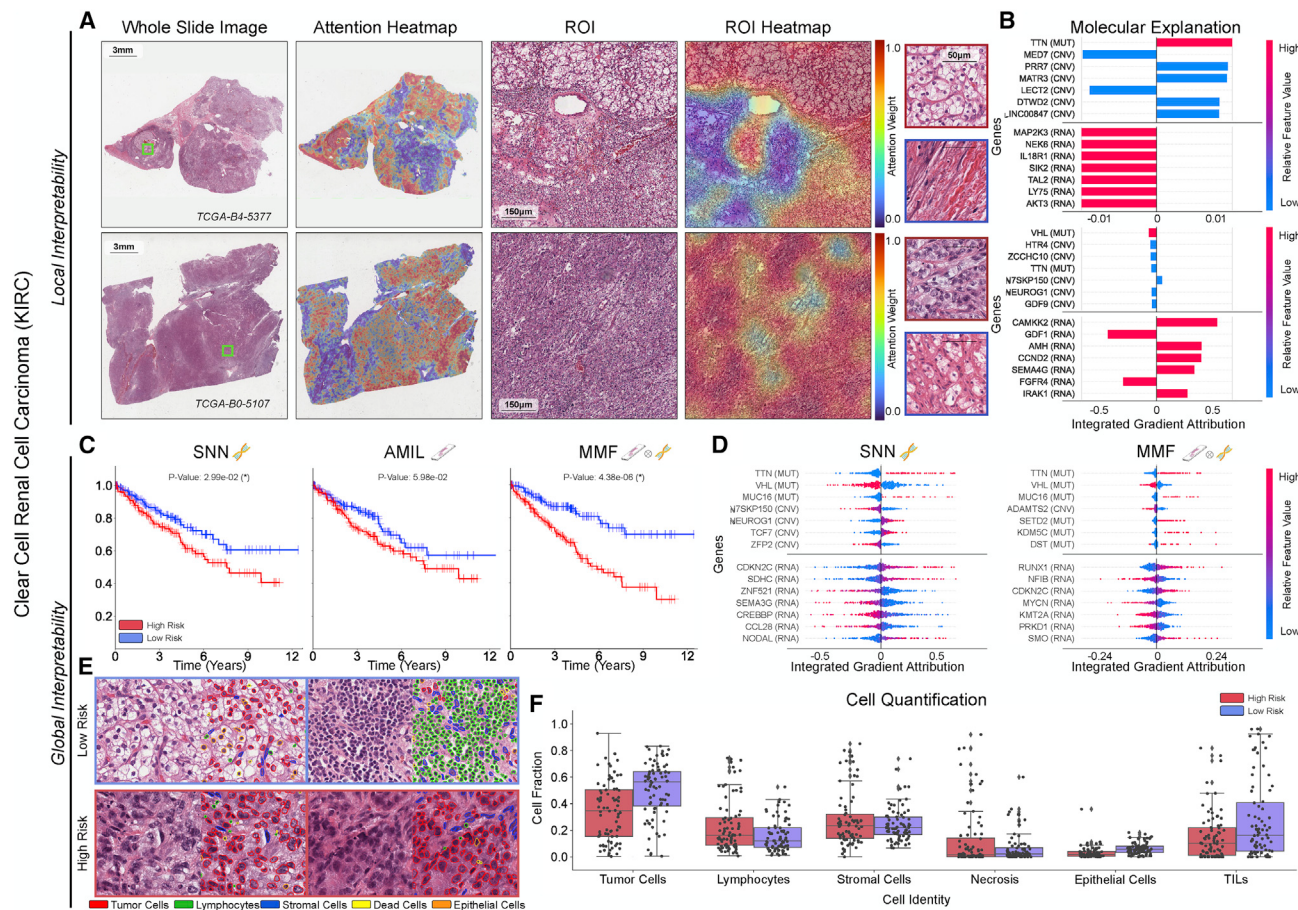


Figure 3. Quantitative performance, local model explanation, and global interpretability analyses of PORPOISE on clear cell renal cell carcinoma (KIRC)

(A) For KIRC ($n = 345$), high attention for low-risk cases (top, $n = 80$) tends to focus on classic clear cell morphology, while in high-risk cases (bottom, $n = 80$), high attention often corresponds to areas with decreased cytoplasm or increased nuclear to cytoplasmic ratio.

(B) Local gene attributions for the corresponding low- (top) and high-risk (bottom) cases.

(C) Kaplan-Meier curves for omics only (left, “SNN”), histology only (center, “AMIL”), and multimodal fusion (right, “MMF”), showing improved separation using MMF. Logrank test was used to test for statistical significance in survival distributions between low- and high-risk patients (with * marked if $p\text{-Value} < 0.05$).

(D) Global gene attributions across patient cohorts according to unimodal interpretability (left, “SNN”) and multimodal interpretability (right, “MMF”). SNN and MMF were both able to identify immune-related and prognostic markers such as CDKN2C and VHL in KIRC. MMF additionally attributes to other immune-related/prognostic genes such as RUNX1 and NFIB in KIRC.

(E) Exemplar high-attention patches from low- (top) and high-risk (bottom) cases with corresponding cell labels.

(F) Quantification of cell types in high-attention patches for each disease overall, showing increased tumor and TIL presence. Boxes indicate quartile values and whiskers extend to data points within $1.5 \times$ the interquartile range.

See also Figures S2–S11 and Table S4.

attribute feature importance to prognostic information in WSIs. Interestingly, WSIs contributed to 32.4% of input attributions in PAAD, despite AMIL performing worse than SNN, which may suggest that MMF is able to extract prognostic morphological features not captured in molecular biomarkers via SNN or unimodal feature extraction via AMIL.

Multimodal interpretability for joint image-omic biomarker discovery

For interpretation and further validation of our models, we applied attention- and gradient-based interpretability to our trained SNN, AMIL, and MMF models in order to explain how WSIs and molecular features are respectively used to predict

prognosis. For WSIs, we used a custom visualization tool that overlays attention weights computed from AMIL (and the AMIL subnetwork from MMF) onto the H&E diagnostic slide, which is displayed as a high-resolution attention heatmap that shows relative prognostic relevance of image regions used to predict risk (Figures 3, 4, 5, and 6A). For molecular features, we used Shapley Additive Explanation (SHAP)-styled attribution decision plots to visualize the attribution weight and direction of each molecular feature calculated by integrated gradients in SNN (and the SNN subnetwork of MMF) (Figures 3, 4, 5, and 6B and 3D, 4D, 5D, and 6D, respectively). These interpretation and visualization techniques were then used to build our discovery platform, PORPOISE, which we then applied to each of our models

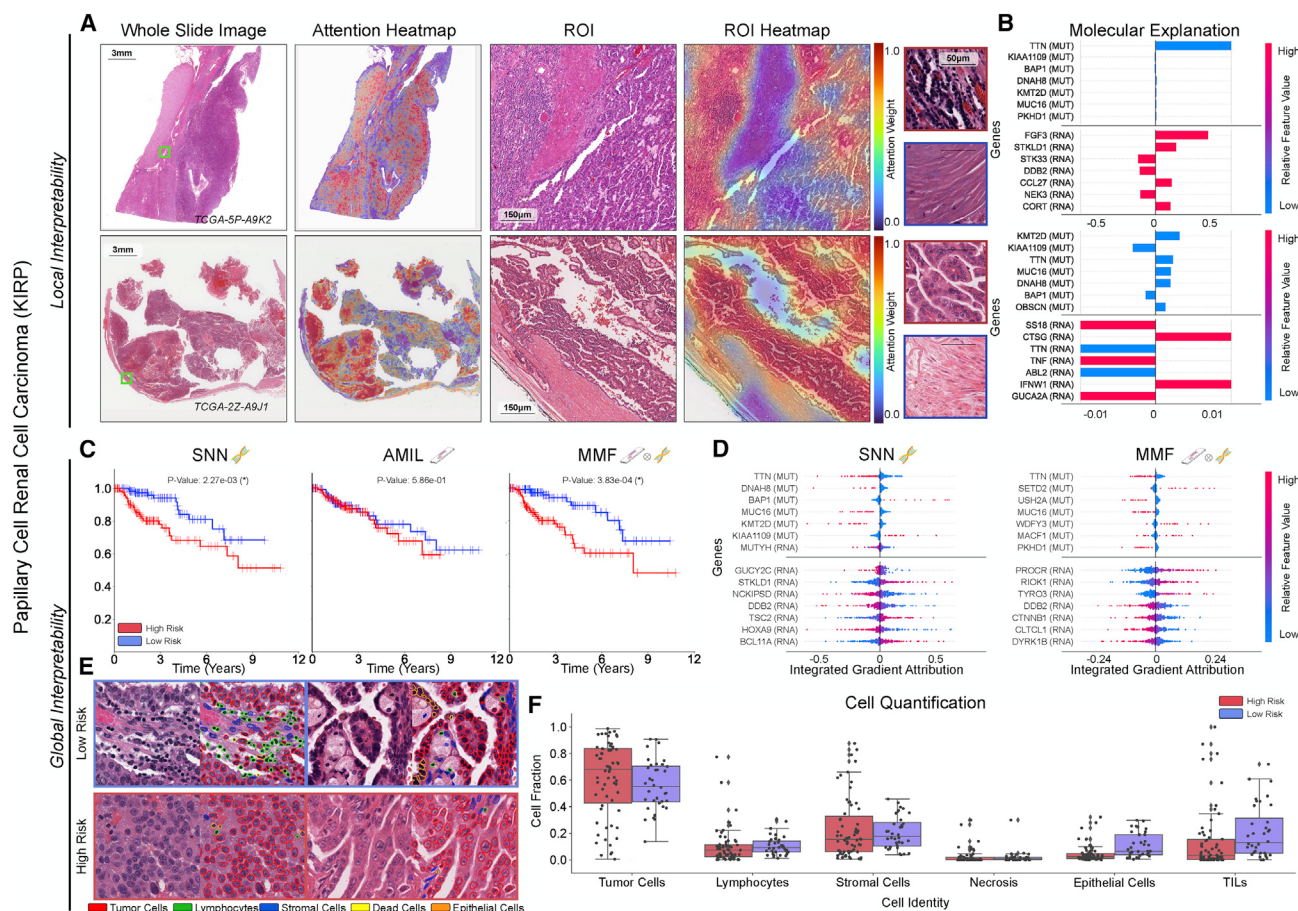


Figure 4. Quantitative performance, local model explanation, and global interpretability analyses of PORPOISE in papillary renal cell carcinoma (KIRP)

(A) For KIRP ($n = 253$), low-risk cases (top, $n = 36$) often have high attention paid to complex and curving papillary architecture, while for high-risk cases (bottom, $n = 63$), high attention is paid to denser areas of tumor cells.

(B) Local gene attributions for the corresponding low- (top) and high-risk (bottom) cases.

(C) Kaplan-Meier curves for omics only (left, “SNN”), histology only (center, “AMIL”), and multimodal fusion (right, “MMF”), showing improved separation using MMF. Logrank test was used to test for statistical significance in survival distributions between low- and high-risk patients (with * marked if p -value < 0.05).

(D) Global gene attributions across patient cohorts according to unimodal interpretability (left, “SNN”) and multimodal interpretability (right, “MMF”). SNN and MMF were both able to identify prognostic markers such as BAP1 in KIRP. MMF additionally attributes to other immune-related/prognostic genes such as PROCR and RIOK1 in KIRP.

(E) Exemplar high-attention patches from low- (top) and high-risk (bottom) cases with corresponding cell labels.

(F) Quantification of cell types in high-attention patches for each disease overall, showing increased epithelial cell and TIL presence. Boxes indicate quartile values and whiskers extend to data points within $1.5 \times$ the interquartile range.

See also Figures S2–S11 and Table S4.

and across all patients, yielding attention heatmaps and attribution decision plots for all 6,592 WSIs and 5,720 patients. Visualizations for analyses for individual patient model explanations in PORPOISE are termed local interpretability, with analyses performed on cancer-wide patient populations termed global interpretability. Figures 3, 4, 5, and 6 show local and global interpretability for KIRC, KIRP, lower grade gliomas (LGGs), and PAAD. Global interpretability results for the rest of the cancer types, as well as local interpretability results are made available in Figures S2–S11.

Patient stratification for unimodal and multimodal prognostic models is shown in Figures 3, 4, 5, 6, 7C, and S2–S11. To obtain an understanding of how morphological features were

used by the model, we assessed high-attention regions of WSIs in the top 25% (high-risk group) and bottom 25% (low-risk group) of predicted patient risks for each cancer type, which reflect favorable and poor cancer prognosis, respectively. In addition to visual inspection from two pathologists, we simultaneously segmented and classified cell-type identities across high-attention regions in our WSIs. Figures 3, 4, 5, and 6A show attention heatmaps with exemplar ROIs for low- and high-risk cases in KIRC, KIRP, LGGs, and PAAD, and Figures 3E, 4E, 5E, and 6E shows semantic segmentation of cell types in high-attention tissue regions in low- and high-risk cases. Figures 3, 4, 5, and 6F compare quantitative cell-type distributions in high-attention patches of low- and

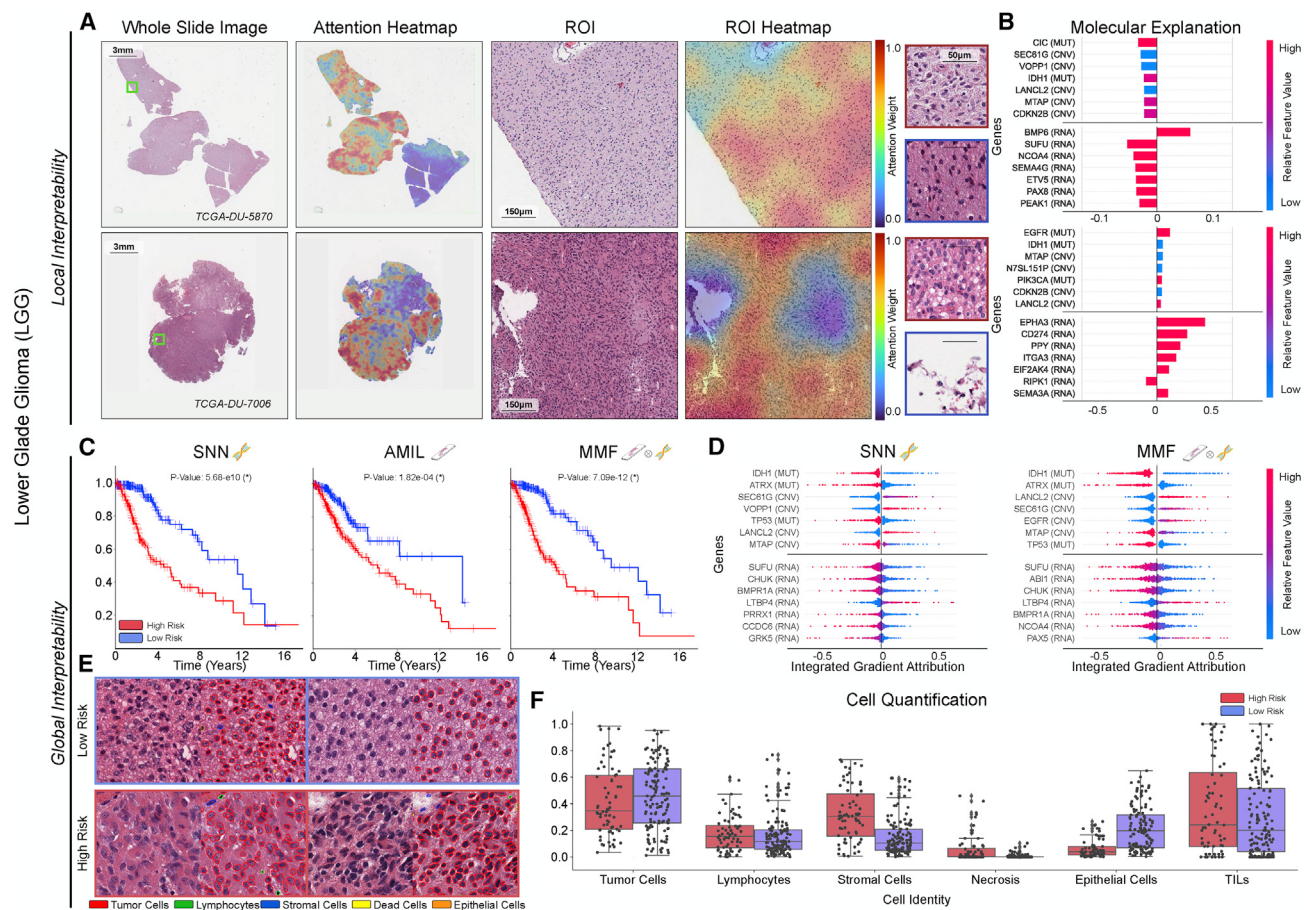


Figure 5. Quantitative performance, local model explanation, and global interpretability analyses of PORPOISE on lower-grade gliomas (LGGs)

- (A) For LGGs ($n = 404$), high attention for low-risk cases (top, $n = 133$) tends to focus on dense regions of tumor cells, while in high-risk cases (bottom, $n = 68$), high attention focuses on both dense regions of tumor cells and areas of vascular proliferation.
- (B) Local gene attributions for the corresponding low- (top) and high-risk (bottom) cases.
- (C) Kaplan-Meier curves for omics only (left, “SNN”), histology only (center, “AMIL”), and multimodal fusion (right, “MMF”), demonstrating improvement in patient stratification in MMF. Logrank test was used to test for statistical significance in survival distributions between low- and high-risk patients (with * marked if p -value < 0.05).
- (D) Global gene attributions across patient cohorts according to unimodal interpretability (left, “SNN”) and multimodal interpretability (right, “MMF”). SNN and MMF were both able to identify immune-related and prognostic markers such as *IDH1*, *ATRX*, *EGFR*, and *CDKN2B* in LGGs.
- (E) High-attention patches from low- (top) and high-risk (bottom) cases with corresponding cell labels, showing oligodendrogloma and astrocytoma subtypes respectively.
- (F) Quantification of cell types in high-attention patches for each disease overall, with statistical significance for increased necrosis in high-risk patients. Boxes indicate quartile values and whiskers extend to data points within $1.5 \times$ the interquartile range.

See also Figures S2–S11 and Table S4.

high-risk cases in these cancer types. Across all cancer types, we generally observed that high-attention regions in low-risk patients corresponded with greater immune cell presence and lower tumor grade than that of high-risk patients, with 8/14 cancer types demonstrating statistically significant differences in lymphocyte cell fractions in high-attention regions (Figures 6F and S3–S10). Furthermore, we also observed that high-attention regions in high-risk patients corresponded with increased tumor cell presence and tumor invasion in certain cancer types, with 6/14 cancer types demonstrating statistically significant differences in tumor cell fractions (Figures S3, S5, S6, S7, S9, and S11). Figures 6F, S3, and S7

show clear differences in cell-fraction distributions in comparing tumor cell fraction (BRCA p: 2.17×10^{-9} , LUAD p: 1.45×10^{-3}) and lymphocyte cell fraction (BRCA p: 6.79×10^{-14} , LUAD p: 1.06×10^{-9} , PAAD p: 2.04×10^{-8} , t test). Figures 3E, 4E, 5E, and 6E show exemplar high-attention regions in low- and high-risk patients, respectively, with attention-based interpretability identifying dense immune cell infiltrates (green) in low-risk patients and nuclear pleomorphism and atypia in tumor cells (red) in high-risk patients. Interestingly, increased fractional tumor cell content in high-attention regions were not discovered in high-risk patients for KIRC and KIRP (Figures 3 and 4F). However, visual inspection of

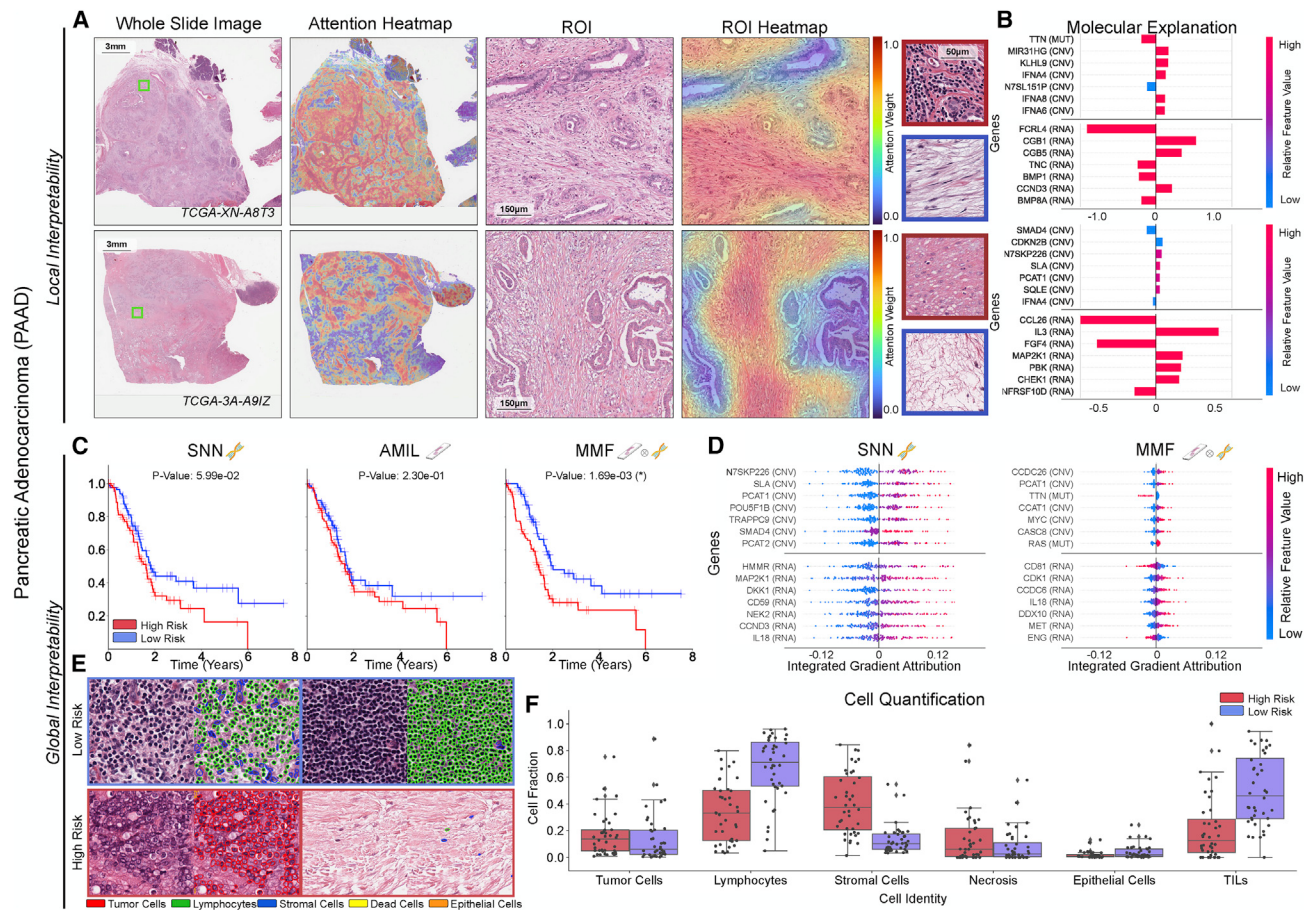


Figure 6. Quantitative performance, local model explanation, and global interpretability analyses of PORPOISE on pancreatic adenocarcinoma (PAAD)

(A) For PAAD ($n = 160$), high attention for low-risk cases (top, $n = 40$) tends to focus on stroma-contained dispersed glands and aggregates of lymphocytes, while in high-risk cases (bottom, $n = 40$), high attention focuses on tumor-associated and myxoid stroma.

(B) Local gene attributions for the corresponding low- (top) and high-risk (bottom) cases from (A) and (G).

(C) Kaplan-Meier curves for omics only (left, “SNN”), histology only (center, “AMIL”), and multimodal fusion (right, “MMF”), demonstrating SNN and AMIL showing poor separation of patients with low survival, with better stratification following multimodal integration. Logrank test was used to test for statistical significance in survival distributions between low- and high-risk patients (with * marked if p -value < 0.05).

(D) Global gene attributions across patient cohorts according to unimodal interpretability (left, “SNN”) and multimodal interpretability (right, “MMF”). SNN and MMF were both able to identify immune-related and prognostic markers such as *IL8*, *EGFR*, and *MET* in PAAD. MMF additionally shifts attribution to other immune-related/prognostic genes such as *CD81*, *CDK1*, and *IL9*.

(E) High-attention patches from low- (top) and high-risk (bottom) cases with corresponding cell labels.

(F) Quantification of cell types in high-attention patches for each disease overall, showing increased lymphocyte and TIL presence in low-risk patients, as well as increased necrosis presence in PAAD. Boxes indicate quartile values and whiskers extend to data points within $1.5 \times$ the interquartile range.

See also Figures S2–S11 and Table S4.

high-attention regions in these cancer types revealed that tumor cells in low-risk patients corresponded with lower tumor grade than that of high-risk patients. Figures 3 and 4A provide examples of attention heatmaps for low- and high-risk patients in KIRC and KIRP, in which high-attention regions in high-risk patients with KIRC corresponded with central necrosis and high-attention regions in high-risk patients with KIRP correspond with tumor cells invading the renal capsule. To understand how attention shifts when conditioning on molecular features in multimodal interpretability, we also had two pathologists use PORPOISE to assess unimodal and multimodal attention heatmaps. For certain cancer types such as BRCA

and KIRC, attention in MMF shifted way from tumor-only regions and toward both stroma and tumor regions, which demonstrates the prognostic relevance of stromal regions (Figure S12) (Beck et al., 2011; Bejnordi et al., 2017).

In parallel with assessing WSI interpretability, we also interrogated important model explanations in our molecular feature inputs. Figures 3, 4, 5, and 6B shows local interpretability and 3D, 4D, 5D, and 6D shows global importance of molecular features for KIRC, KIRP, LGGs, and PAAD. Across all cancer types, gradient-based interpretability was able to identify many well-known oncogenes and immune-related genes established in existing biomedical literature and used in targeted molecular

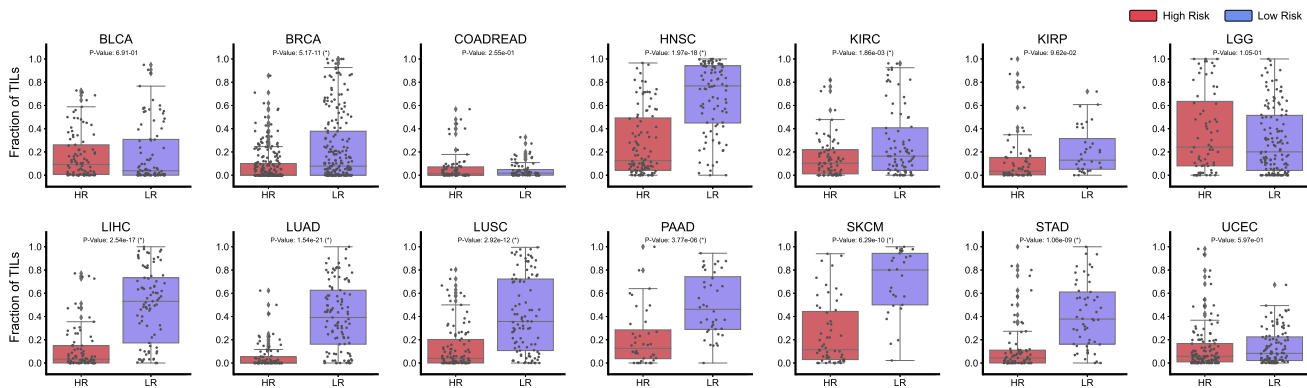


Figure 7. TIL quantification in patient risk groups

TIL quantification in high-attention regions of predicted low- (BLCA n = 90, BRCA n = 220, COADREAD n = 74, HNSC n = 96, KIRC n = 80, KIRP n = 36, LGG n = 133, LIHC n = 85, LUAD n = 105, LUSC n = 97, PAAD n = 40, SKCM n = 29, STAD n = 53, UCEC = 104) and high-risk patient cases (BLCA n = 93, BRCA n = 223, COADREAD n = 80, HNSC n = 103, KIRC n = 80, KIRP n = 63, LGG n = 68, LIHC n = 84, LUAD n = 89, LUSC n = 103, PAAD n = 40, SKCM n = 55, STAD n = 78, UCEC = 125) across 14 cancer types. For each patient, the top 1% of scored high-attention regions (512×512 40x image patches) were segmented and analyzed for tumor and immune cell presence. Image patches with high tumor-immune co-localization were indicated as positive for TIL presence (and negative otherwise). Across all patients, the fraction of high-attention patches containing TIL presence was computed and visualized in the boxplots. A two-sample t test was computed for each cancer type to test the if the means of the TIL fraction distributions of low- and high-risk patients had a statistically significant difference (* $p < 0.05$). Boxes indicate quartile values and whiskers extend to data points within $1.5 \times$ the interquartile range.

therapies (Uhlen et al., 2017). In the LGG cohort, which has distinct molecular signatures, gradient-based interpretability identifies *IDH1* mutation ($p: 2.31 \times 10^{-89}$, t test) status as the most attributed gene feature, which has important functions in cellular metabolism, epigenetic regulation, and DNA repair and defines the *IDH1*-wild-type astrocytoma, *IDH1*-mutant astrocytoma, and *IDH1*-mutant oligodendrogloma molecular subtypes (Louis et al., 2016). In addition, *IDH1* mutation is associated with LGGs and thus favorable prognosis compared with *IDH1*-wild-type gliomas, which successfully corroborates with the attribution direction of *IDH1* mutation in the attribution decision plot, in which the distribution of *IDH1* mutation attributions has only negative attribution values (low risk) (Figure 5D). The model also uses several other key oncogenes in other cancer types such as *PIK3CA* mutation ($p: 4.04 \times 10^{-18}$, t test) in BRCA, *SOX9* mutation ($p: 7.56 \times 10^{-64}$, t test), and *SOX11* mutation ($p: 1.65 \times 10^{-58}$, t test) in COADREAD; *KRAS* mutation in LUAD ($p: 1.98 \times 10^{-63}$, t test) and PAAD ($p: 9.00 \times 10^{-12}$, t test); and *VHL* ($p: 1.76 \times 10^{-62}$, t test) and *BAP1* ($p: 5.57 \times 10^{-18}$, t test) mutations in KIRC (Figures 3D, 5D, S3, and S6). In PAAD, we additionally observe attributions of immune-related genes, such as *CD81*, *CDK1*, *IL8*, and *IL9*, whose RNA-seq expressions are found to be the most highly attributed, which corroborates with their roles in innate immunity and inflammatory cell signaling (Cancer Genome Atlas Research Network, 2013; Uhlen et al., 2015; Chevrier et al., 2017; Uhlen et al., 2017, 2019) (Figure 6D). Moreover, we note that, following conditioning on WSIs, MMF models for PAAD show a relative decrease in attribution for many genes, which corroborates with our previous observation of much higher WSI attribution in PAAD for MMF patient stratification. Across most cancer types, gene mutations that encode for extremely large proteins such as *TTN*, *OBSCN*, *RYR3*, and *DNA5* were frequently found to be highly attributed. Though many of these genes are not explicitly cancer-associated and prognostic due to heterogeneity in the mutational processes of each cancer type, genomic instabilities

in these large protein-coding domains may be an indirect measure of tumor mutational load (Lawrence et al., 2013; Rizvi et al., 2015; Shi et al., 2021; Oh et al., 2020). Attributions for all gene features for SNN and MMF can be found in Table S4.

Immune response as a prognostic marker

Lastly, we used the interpretability of PORPOISE as a mechanism to test the hypothesis that tumor-infiltrating lymphocyte (TIL) presence corroborates with favorable cancer prognosis. Figure 7 shows the fractional distribution of TILs in the high-attention regions for all 14 cancer types across the previously defined risk groups. In comparing TIL presence between low- and high-risk patients, we found that 9 out of 14 cancer types had a statistically significant increase in TIL presence among patients with predicted low risk, indicating that model attention was localized to more immune-hot regions. For cancer types in our dataset that are commonly treated with FDA-approved immune checkpoint inhibitor therapies, TIL presence was used as a model explanation for favorable prognosis in BRCA ($p: 5.17 \times 10^{-11}$, t test); HNSC ($p: 1.97 \times 10^{-18}$, t test); KIRC ($p: 1.86 \times 10^{-3}$, t test); LIHC ($p: 2.54 \times 10^{-17}$, t test); LUAD ($p: 1.54 \times 10^{-21}$, t test); LUSC ($p: 2.92 \times 10^{-12}$, t test); PAAD ($p: 3.77 \times 10^{-6}$, t test); STAD ($p: 1.09 \times 10^{-9}$, t test); and SKCM ($p: 6.29 \times 10^{-10}$, t test). This suggests that our trained models use morphological features for immune response as markers for predicting cancer prognosis and supports a growing body of evidence that TILs have a prognostic role in many cancer types (Thorsson et al., 2018; Saltz et al., 2018; Shaban et al., 2019; AbdulJabbar et al., 2020). In BRCA, Maley et al. performed hotspot analysis on the co-localization of immune cancer cells in WSIs and showed that immune-cancer co-localization was a significant predictive factor of long-term survival (Maley et al., 2015). In oral squamous cell carcinoma, Shaban et al. proposed a co-localization score for quantifying TIL density that showed similar findings (Shaban et al., 2019). In lung cancer, AbdulJabbar et al. proposed a deep-learning framework for

spatially profiling immune infiltration in H&E and immunohistochemistry (IHC) WSIs and similarly found that tumors with more than one immune cold region had a higher risk of relapse (AbdulJabbar et al., 2020). Saltz et al. performed a pan-cancer analysis on the spatial organization of TILs in the TCGA and showed how different phenotypes of TIL infiltrates correlate with survival (Saltz et al., 2018). The distinction of these analyses compared with PORPOISE is that our method is not specifically trained in identifying TILs and correlating TILs with outcome. Rather, dissection of model interpretability reveals that TIL presence is used as prognostic morphological features in stratifying low- and high-risk patients.

DISCUSSION

There is much promise that incorporating computationally derived, histomorphological biomarkers into clinical staging systems will allow for better risk stratification of patients (Echle et al., 2021; Bera et al., 2019). Current cancer staging systems, such as the TNM classification system, struggle with precision and consistency, leading to subsequent variation in patient management and outcomes (Nicholson et al., 2001; Novara et al., 2007; Rabe et al., 2019). In this study, we present a method for interpretable, weakly supervised, multimodal deep learning that integrates WSIs and molecular profile data for cancer prognosis, which we trained and validated on 6,592 WSIs from 5,720 patients with paired molecular profile data across 14 cancer types, and compared our method with unimodal deep-learning models as well as Cox models with clinical covariates, achieving the highest c-Index performance on 12 out of 14 cancer types in a one-versus-all comparison. Our method also explores multimodal interpretability in explaining how features from WSIs and molecular features contribute toward risk. We developed PORPOISE, an interactive, freely available platform that directly yields both WSI and molecular feature explanations made by our model in our 14 cancer types. Our goal with PORPOISE is to begin making current black-box state-of-the-art methods in computational pathology, especially emerging multimodal methods, more transparent, explainable, and usable for the broader biomedical research community. In making heatmaps and decision plots available for each cancer type, we hope that our tool would allow clinicians and researchers to devise their own hypotheses and investigate the discoveries explained using deep learning.

Though we find that multimodal integration benefits patient risk stratification for most cancer types, our results also suggest that for some cancer types, training unimodal algorithms using either WSIs or molecular features alone may achieve comparable stratification performance, as variance of cancer outcomes can be equally captured in either modality. Many practical settings may lack paired diagnostic slide or high-throughput sequencing data for the same tissue specimen, and here, unimodal deep-learning-based cancer-prognosis algorithms may have reduced barriers to clinical deployment. Though multimodal learning has been successful in technical domains such as the integration of audio, visual, and language modalities, for clinical translational tasks, we note that the basis of improvement from multimodal integration needs to be grounded in the biology of each cancer type, as phenotypic manifestations in the tumor microenvironment that are entirely explained by contri-

butions from genotype have high mutual information (Kather et al., 2020). In establishing unimodal and multimodal baselines for 14 diverse cancer types, our results advocate that the application of multimodal integration should be determined on a per-cancer basis, which may aid in introspecting clinical problems for unimodal or multimodal biomarkers on single disease models.

A limitation of our approach is that though our approach can point to “what” and “where,” it cannot always explain “why” for discovered features that must be further quantified and introspected based on human knowledge. For example, though TILs were found in most cancer types to distinguish low- and high-risk patients, post hoc analyses still had to be done to quantify TIL presence and assess statistical significance between the two risk groups. In analyses on feature shift in WSIs, we observe that high attention often shifted away from tumor regions to stroma, normal tissue, and other morphological regions in some cancer types. We speculate this observation is a result of the intrinsic differences between WSIs and molecular profile data, in which training dynamics may be biased toward using more information from the simpler modality (Wang et al., 2020). In molecular features, the genotypic information from gene mutation, copy-number variation, and RNA-seq abundances that have no spatial resolution are averaged across cells in the tumor biopsies, whereas phenotypic information such as normal tissue, tumor cells, and other morphological determinants are spatially represented in WSIs. As a result, when our multimodal algorithm is already conditioned with tumor-related features (e.g., TP53 mutation status, PTEN loss) in the molecular profile, it can attend to morphological regions with non-tumor information such as stroma to explain subtle differences in survival outcomes (Beck et al., 2011). In other words, feature importance does not need to be attributed to oncogenes in molecular features and tumor-containing image regions in WSIs that have high collinearity, which allows the multimodal network to learn other histology-specific prognostic information beyond tumor grades.

In addition to characterizing known human-identifiable phenotypes such as TILs in cancer, PORPOISE can potentially be used by the research community in further characterization of phenotypes that are currently not well understood via robust quantification of cell-type populations and tissue architecture (Diao et al., 2021). Moreover, multimodal networks for general disease prognostication and outcome prediction adapted to larger and well-curated clinical trial data can be used to aid in both discovery and validation of human-interpretable image-omic biomarkers in guiding treatment decisions. Tangential research directions in similar pursuit of this goal are the prediction of molecular biomarkers from WSIs and other genotype-phenotype correlations, which would decrease the complexity of routine clinical workflows that require molecular assays for therapeutic decision-making. While this approach has the potential to elucidate morphological markers that would predict molecular aberrations, there may exist orthogonal morphological biomarkers that are prognostic but do not have correlation with molecular features. As observed in PAAD, though AMIL is not prognostic for survival outcomes and performs worse than SNN, we demonstrate not only performance increase in multimodal integration but also relatively high attribution given to WSIs, suggesting the existence of prognostic information not currently captured

using molecular features or unimodal feature extraction in WSIs. On the other hand, in cancer types such as BRCA, COADREAD, and LUAD, which benefit from multimodal integration, MMF models have lower attribution given to WSIs, which may result from prognostic information also partially explained via genomics as aberrations such as *ERBB2* or *KRAS* mutation, and the presence of microsatellite instability can be determined from histology (Coudray et al., 2018; Kather et al., 2019a, 2019b, 2020; Gamble et al., 2021). Toward the development of computational support systems for therapeutic decision-making, further work in genotype-phenotype correlation-based analyses would develop more formal intuition in understanding shared and modality-specific prognostic information for multimodal integration-based approaches, which may lead to clinical validation of either single-modality or joint image-omic computational biomarkers (per cancer type) for downstream prognostication.

Overall, this study is a proof of concept showing the development multimodal prognostic models from orthogonal data streams using weakly supervised deep learning and subsequently identifying correlative features that drive such prognosis. Future work will focus on developing more focused prognostic models by curating larger multimodal datasets for individual disease models, adapting models to large independent multimodal test cohorts, and using multimodal deep learning for predicting response and resistance to treatment. As research advances in sequencing technologies such as single-cell RNA-seq, mass cytometry, and spatial transcriptomics, these technologies continue to mature and gain clinical penetrance, in combination with whole-slide imaging, and our approach to understanding molecular biology will become increasingly spatially resolved and multimodal (Abdelmoula et al., 2016; Berglund et al., 2018; Giesen et al., 2014; Jackson et al., 2020; Schapiro et al., 2017; He et al., 2020). In using bulk molecular profile data, our multimodal learning algorithm is considered a “late fusion” architecture, in which unimodal WSIs and molecular features are fused near the output end of the network (Baltrušaitis et al., 2018). However, spatially resolved genomics and transcriptomics data in combination with whole-slide imaging have the potential to enable “early fusion” deep-learning techniques that integrate local histopathology image regions and molecular features with exact spatial correspondences, which will lead to more robust characterizations and spatial organization mappings of intratumoral heterogeneity, immune cell presence, and other morphological determinants.

STAR★METHODS

Detailed methods are provided in the online version of this paper and include the following:

- KEY RESOURCES TABLE

- RESOURCE AVAILABILITY

- Lead contact
- Materials availability
- Data and code availability

- METHOD DETAILS

- Dataset description
- WSI processing

- Deep learning-based survival analysis for integrating whole slide images and genomic features
- Multimodal interpretability and visualization
- Computational hardware and software

- QUANTIFICATION AND STATISTICAL ANALYSIS

SUPPLEMENTAL INFORMATION

Supplemental information can be found online at <https://doi.org/10.1016/j.ccr.2022.07.004>.

ACKNOWLEDGMENTS

This work was supported in part by BWH President's Fund, MGH Pathology, Google Cloud Research Grant, Nvidia GPU Grant Program, and NIGMS R35GM138216 (to F.M.). R.J.C. was additionally supported by the National Science Foundation (NSF) Graduate Fellowship. M.S. was additionally supported by the National Institutes of Health (NIH) National Library of Medicine (NLM) Biomedical Informatics and Data Science Research Training Program, T15LM007092. M.W. was additionally supported by the NIH National Human Genome Research Institute (NHGRI) Ruth L. Kirschstein National Research Service Award Bioinformatics Training Grant, T32HG002295. T.Y.C. was additionally supported by the NIH National Cancer Institute (NCI) Ruth L. Kirschstein National Service Award, T32CA251062. The content is solely the responsibility of the authors and does not reflect the official views of the NIH, NIGMS, NHGRI, NLM, NSF or the NCI.

AUTHOR CONTRIBUTIONS

R.J.C. and F.M. conceived the study and designed the experiments. R.J.C. and M.Y.L. performed the experimental analysis. All authors contributed to data analysis and interpretation. R.J.C., M.Y.L., M.W., M.S., and Z.N. developed data visualization tools. R.J.C., D.F.K.W., T.Y.C., and F.M. interpreted and analyzed the results. R.J.C. and F.M. prepared the manuscript with input and feedback from all co-authors. F.M. supervised the research.

DECLARATION OF INTERESTS

R.J.C. and F.M. are inventors on a patent that has been filed corresponding multimodal data fusion using deep learning. The authors declare no other competing interests.

Received: June 24, 2021

Revised: October 8, 2021

Accepted: July 11, 2022

Published: August 8, 2022

REFERENCES

- Abdelmoula, W.M., Balluff, B., Englert, S., Dijkstra, J., Reinders, M.J.T., Walch, A., McDonnell, L.A., and Lelieveldt, B.P.F. (2016). Data-driven identification of prognostic tumor subpopulations using spatially mapped t-SNE of mass spectrometry imaging data. Proc. Natl. Acad. Sci. USA 113, 12244–12249. <https://doi.org/10.1073/pnas.1510227113>.
- AbdulJabbar, K., Raza, S.E.A., Rosenthal, R., Jamal-Hanjani, M., Veeriah, S., Akarca, A., Lund, T., Moore, D.A., Salgado, R., Al Bakir, M., et al. (2020). Geospatial immune variability illuminates differential evolution of lung adenocarcinoma. Nat. Med. 26, 1054–1062. <https://doi.org/10.1038/s41591-020-0900-x>.
- Amin, M.B., Greene, F.L., Edge, S.B., Compton, C.C., Gershensonwald, J.E., Brookland, R.K., Meyer, L., Gress, D.M., Byrd, D.R., and Winchester, D.P. (2017). The eighth edition AJCC cancer staging manual: continuing to build a bridge from a population-based to a more “personalized” approach to cancer staging. CA. Cancer J. Clin. 67, 93–99. <https://doi.org/10.3322/caac.21388>.
- Bai, H., Harmancı, A.S., Erson-Omay, E.Z., Li, J., Coşkun, S., Simon, M., Krischek, B., Özduuman, K., Omay, S.B., Sorensen, E.A., et al. (2016).

- Integrated genomic characterization of IDH1-mutant glioma malignant progression. *Nat. Genet.* 48, 59–66. <https://doi.org/10.1038/ng.3457>.
- Baltrušaitis, T., Ahuja, C., and Morency, L.P. (2019). Multimodal machine learning: a survey and taxonomy. *IEEE Trans. Pattern Anal. Mach. Intell.* 41, 423–443. <https://doi.org/10.1109/tpami.2018.2798607>.
- Beck, A.H., Sangoi, A.R., Leung, S., Marinelli, R.J., Nielsen, T.O., Van De Vijver, M.J., West, R.B., Van De Rijn, M., and Koller, D. (2011). Systematic analysis of breast cancer morphology uncovers stromal features associated with survival. *Sci. Transl. Med.* 3, 108ra113. <https://doi.org/10.1126/scitranslmed.3002564>.
- Bejnordi, B.E., Lin, J., Glass, B., Mullooly, M., Gierach, G.L., Sherman, M.E., Karssemeijer, N., Van Der Laak, J., and Beck, A.H. (2017). April. Deep learning-based assessment of tumor-associated stroma for diagnosing breast cancer in histopathology images. In 2017 IEEE 14th International Symposium on Biomedical Imaging (IEEE), pp. 929–932. ISBI 2017. <https://doi.org/10.1109/isbi.2017.7950668>.
- Bera, K., Schalper, K.A., Rimm, D.L., Velcheti, V., and Madabhushi, A. (2019). Artificial intelligence in digital pathology—new tools for diagnosis and precision oncology. *Nat. Rev. Clin. Oncol.* 16, 703–715. <https://doi.org/10.1038/s41571-019-0252-y>.
- Berglund, E., Maaskola, J., Schultz, N., Friedrich, S., Marklund, M., Bergensträhle, J., Tarish, F., Tanoglidı, A., Vickovic, S., Larsson, L., et al. (2018). Spatial maps of prostate cancer transcriptomes reveal an unexplored landscape of heterogeneity. *Nat. Commun.* 9, 2419–2513. <https://doi.org/10.1038/s41467-018-04724-5>.
- Bland, J.M., and Altman, D.G. (2004). The logrank test. *Bmj* 328, 1073. <https://doi.org/10.1136/bmj.328.7447.1073>.
- Campanella, G., Hanna, M.G., Geneslaw, L., Miraflor, A., Werneck Krauss Silva, V., Busam, K.J., Brogi, E., Reuter, V.E., Klimstra, D.S., and Fuchs, T.J. (2019). Clinical-grade computational pathology using weakly supervised deep learning on whole slide images. *Nat. Med.* 25, 1301–1309. <https://doi.org/10.1038/s41591-019-0508-1>.
- Chang, H., Borowsky, A., Spellman, P., and Parvin, B. (2013). Classification of tumor histology via morphometric context. In Proceedings of the IEEE Conference on Computer Vision and Pattern Recognition, pp. 2203–2210. <https://doi.org/10.1109/cvpr.2013.286>.
- Chen, R.J., Lu, M.Y., Wang, J., Williamson, D.F.K., Rodig, S.J., Lindeman, N.I., and Mahmood, F. (2020). Pathomic fusion: an integrated framework for fusing histopathology and genomic features for cancer diagnosis and prognosis. *IEEE Trans. Med. Imaging* 41, 757–770. <https://doi.org/10.1109/tmi.2020.3021387>.
- Cheerla, A., and Gevaert, O. (2019). Deep learning with multimodal representation for pancancer prognosis prediction. *Bioinformatics* 35, i446–i454. <https://doi.org/10.1093/bioinformatics/btz342>.
- Chevrier, S., Levine, J.H., Zanotelli, V.R.T., Silina, K., Schulz, D., Bacac, M., Ries, C.H., Ailles, L., Jewett, M.A.S., Moch, H., et al. (2017). An immune atlas of clear cell renal cell carcinoma. *Cell* 169, 736–749.e18. <https://doi.org/10.1016/j.cell.2017.04.016>.
- Cloughesy, T.F., Mochizuki, A.Y., Orpilla, J.R., Hugo, W., Lee, A.H., Davidson, T.B., Wang, A.C., Ellingson, B.M., Rytlewski, J.A., Sanders, C.M., et al. (2019). Neoadjuvant anti-PD-1 immunotherapy promotes a survival benefit with intratumoral and systemic immune responses in recurrent glioblastoma. *Nat. Med.* 25, 477–486. <https://doi.org/10.1038/s41591-018-0337-7>.
- Coudray, N., Ocampo, P.S., Sakellaropoulos, T., Narula, N., Snuderl, M., Fenyö, D., Moreira, A.L., Razavian, N., and Tsirigos, A. (2018). Classification and mutation prediction from non-small cell lung cancer histopathology images using deep learning. *Nat. Med.* 24, 1559–1567. <https://doi.org/10.1038/s41591-018-0177-5>.
- Courtial, P., Maussion, C., Moarii, M., Pronier, E., Pilcer, S., Sefta, M., Manceron, P., Toldo, S., Zaslavskiy, M., Le Stang, N., et al. (2019). Deep learning-based classification of mesothelioma improves prediction of patient outcome. *Nat. Med.* 25, 1519–1525. <https://doi.org/10.1038/s41591-019-0583-3>.
- Diao, J.A., Wang, J.K., Chui, W.F., Mountain, V., Gullapally, S.C., Srinivasan, R., Mitchell, R.N., Glass, B., Hoffman, S., Rao, S.K., et al. (2021). Human-interpretable image features derived from densely mapped cancer pathology slides predict diverse molecular phenotypes. *Nat. Commun.* 12, 1613–1615. <https://doi.org/10.1038/s41467-021-21896-9>.
- Echle, A., Rindtorff, N.T., Brinker, T.J., Luedde, T., Pearson, A.T., and Kather, J.N. (2021). Deep learning in cancer pathology: a new generation of clinical biomarkers. *Br. J. Cancer* 124, 686–696. <https://doi.org/10.1038/s41416-020-01122-x>.
- Fridman, W.H., Zitvogel, L., Sautès-Fridman, C., and Kroemer, G. (2017). The immune contexture in cancer prognosis and treatment. *Nat. Rev. Clin. Oncol.* 14, 717–734. <https://doi.org/10.1038/nrclinonc.2017.101>.
- Fu, Y., Jung, A.W., Torne, R.V., Gonzalez, S., Vöhringer, H., Shmatko, A., Yates, L.R., Jimenez-Linan, M., Moore, L., and Gerstung, M. (2020). Pan-cancer computational histopathology reveals mutations, tumor composition and prognosis. *Nat. Cancer* 1, 800–810. <https://doi.org/10.1038/s43018-020-0085-8>.
- Gamble, P., Jaroensri, R., Wang, H., Tan, F., Moran, M., Brown, T., Flament-Auvigne, I., Rakha, E.A., Toss, M., Dabbs, D.J., et al. (2021). Determining breast cancer biomarker status and associated morphological features using deep learning. *Commun. Med.* 1, 14–22. <https://doi.org/10.1038/s43856-021-00013-3>.
- Gentzler, R.D., Yentz, S.E., Johnson, M.L., Rademaker, A.W., and Patel, J.D. (2014). The changing landscape of phase II/III metastatic NSCLC clinical trials and the importance of biomarker selection criteria. *Cancer* 120, 3853–3858. <https://doi.org/10.1002/cncr.28956>.
- Giesen, C., Wang, H.A.O., Schapiro, D., Zivanovic, N., Jacobs, A., Hattendorf, B., Schüffler, P.J., Grolimund, D., Buhmann, J.M., Brandt, S., et al. (2014). Highly multiplexed imaging of tumor tissues with subcellular resolution by mass cytometry. *Nat. Methods* 11, 417–422. <https://doi.org/10.1038/nmeth.2869>.
- Graham, S., Vu, Q.D., Raza, S.E.A., Azam, A., Tsang, Y.W., Kwak, J.T., and Rajpoot, N. (2019). Hover-net: simultaneous segmentation and classification of nuclei in multi-tissue histology images. *Med. Image Anal.* 58, 101563. <https://doi.org/10.1016/j.media.2019.101563>.
- Harder, N., Schönmeyer, R., Nekolla, K., Meier, A., Brieu, N., Vanegas, C., Madonna, G., Capone, M., Botti, G., Ascierto, P.A., and Schmidt, G. (2019). Automatic discovery of image-based signatures for ipilimumab response prediction in malignant melanoma. *Sci. Rep.* 9, 7449–7519. <https://doi.org/10.1038/s41598-019-43525-8>.
- He, B., Bergensträhle, L., Stenbeck, L., Abid, A., Andersson, A., Borg, Å., Maaskola, J., Lundeberg, J., and Zou, J. (2020). Integrating spatial gene expression and breast tumour morphology via deep learning. *Nat. Biomed. Eng.* 4, 827–834. <https://doi.org/10.1038/s41551-020-0578-x>.
- Heindl, A., Nawaz, S., and Yuan, Y. (2015). Mapping spatial heterogeneity in the tumor microenvironment: a new era for digital pathology. *Lab. Invest.* 95, 377–384. <https://doi.org/10.1038/labinvest.2014.155>.
- Hyman, D.M., Solit, D.B., Arcila, M.E., Cheng, D.T., Sabbatini, P., Baselga, J., Berger, M.F., and Ladanyi, M. (2015). Precision medicine at Memorial Sloan Kettering Cancer Center: clinical next-generation sequencing enabling next-generation targeted therapy trials. *Drug Discov. Today* 20, 1422–1428. <https://doi.org/10.1016/j.drudis.2015.08.005>.
- Ilse, M., Tomczak, J., and Welling, M. (2018). Attention-based deep multiple instance learning. In *International Conference on Machine Learning*, 80, pp. 2127–2136.
- Jackson, H.W., Fischer, J.R., Zanotelli, V.R.T., Ali, H.R., Mechera, R., Soysal, S.D., Moch, H., Muenst, S., Varga, Z., Weber, W.P., and Bodenmiller, B. (2020). The single-cell pathology landscape of breast cancer. *Nature* 578, 615–620. <https://doi.org/10.1038/s41586-019-1876-x>.
- Kather, J.N., Heij, L.R., Grabsch, H.I., Loeffler, C., Echle, A., Muti, H.S., Krause, J., Niehues, J.M., Sommer, K.A.J., Bankhead, P., et al. (2020). Pan-cancer image-based detection of clinically actionable genetic alterations. *Nat. Cancer* 1, 789–799. <https://doi.org/10.1038/s43018-020-00087-6>.
- Kather, J.N., Suarez-Carmona, M., Charoentong, P., Weis, C.A., Hirsch, D., Bankhead, P., Horning, M., Ferber, D., Kel, I., Herpel, E., et al. (2018). Topography of cancer-associated immune cells in human solid tumors. *Elife* 7, e36967. <https://doi.org/10.7554/elife.36967>.

- Kather, J.N., Krisam, J., Charoentong, P., Luedde, T., Herpel, E., Weis, C.A., Gaiser, T., Marx, A., Valous, N.A., Ferber, D., et al. (2019a). Predicting survival from colorectal cancer histology slides using deep learning: a retrospective multicenter study. *PLoS Med.* 16, e1002730. <https://doi.org/10.1371/journal.pmed.1002730>.
- Kather, J.N., Pearson, A.T., Halama, N., Jäger, D., Krause, J., Loosen, S.H., Marx, A., Boor, P., Tacke, F., Neumann, U.P., et al. (2019b). Deep learning can predict microsatellite instability directly from histology in gastrointestinal cancer. *Nat. Med.* 25, 1054–1056. <https://doi.org/10.1038/s41591-019-0462-y>.
- Klambauer, G., Unterthiner, T., Mayr, A., and Hochreiter, S. (2017). Self-normalizing neural networks. *Adv. Neural Inf. Process. Syst.* 30.
- Kokhlikyan, N., Miglani, V., Martin, M., Wang, E., Alsallakh, B., Reynolds, J., Melnikov, A., Kliushkina, N., Araya, C., Yan, S., and Reblitz-Richardson, O. (2020). Captum: a unified and generic model interpretability library for pytorch. Preprint at arXiv. <https://doi.org/10.48550/arXiv.2009.07896>.
- Kulkarni, P.M., Robinson, E.J., Sarin Pradhan, J., Gartrell-Corradò, R.D., Rohr, B.R., Trager, M.H., Geskin, L.J., Kluger, H.M., Wong, P.F., Acs, B., et al. (2020). Deep learning based on standard H&E images of primary melanoma tumors identifies patients at risk for visceral recurrence and death. *Clin. Cancer Res.* 26, 1126–1134. <https://doi.org/10.1158/1078-0432.ccr-19-1495>.
- Lawrence, M.S., Stojanov, P., Polak, P., Kryukov, G.V., Cibulskis, K., Sivachenko, A., Carter, S.L., Stewart, C., Mermel, C.H., Roberts, S.A., et al. (2013). Mutational heterogeneity in cancer and the search for new cancer-associated genes. *Nature* 499, 214–218. <https://doi.org/10.1038/nature12213>.
- LeDell, E., Petersen, M., and van der Laan, M. (2015). Computationally efficient confidence intervals for cross-validated area under the ROC curve estimates. *Electron. J. Stat.* 9, 1583–1607. <https://doi.org/10.1214/15-ejs1035>.
- Liu, Z., Shen, Y., Lakshminarayanan, V.B., Liang, P.P., Bagher Zadeh, A., and Morency, L.-P. (2018). Efficient Low-Rank Multimodal Fusion with Modality-specific Factors (Association for Computational Linguistics). <https://doi.org/10.18653/v1/P18-1209>.
- Louis, D.N., Perry, A., Reifenberger, G., Von Deimling, A., Figarella-Branger, D., Cavenee, W.K., Ohgaki, H., Wiestler, O.D., Kleihues, P., and Ellison, D.W. (2016). The 2016 World Health Organization classification of tumors of the central nervous system: a summary. *Acta Neuropathol.* 131, 803–820. <https://doi.org/10.1007/s00401-016-1545-1>.
- Lu, M.Y., Williamson, D.F.K., Chen, T.Y., Chen, R.J., Barbieri, M., and Mahmood, F. (2021). Data-efficient and weakly supervised computational pathology on whole-slide images. *Nat. Biomed. Eng.* 5, 555–570. <https://doi.org/10.1038/s41551-020-00682-w>.
- Ludwig, J.A., and Weinstein, J.N. (2005). Biomarkers in cancer staging, prognosis and treatment selection. *Nat. Rev. Cancer* 5, 845–856. <https://doi.org/10.1038/nrc1739>.
- Lundberg, S.M., Erion, G., Chen, H., DeGrave, A., Prutkin, J.M., Nair, B., Katz, R., Himmelfarb, J., Bansal, N., and Lee, S.I. (2020). From local explanations to global understanding with explainable AI for trees. *Nat. Mach. Intell.* 2, 56–67. <https://doi.org/10.1038/s42256-019-0138-9>.
- Maley, C.C., Koelble, K., Natrajan, R., Aktipis, A., and Yuan, Y. (2015). An ecological measure of immune-cancer colocalization as a prognostic factor for breast cancer. *Breast Cancer Res.* 17, 131–213. <https://doi.org/10.1186/s13058-015-0638-4>.
- Marusyk, A., Almendro, V., and Polyak, K. (2012). Intra-tumour heterogeneity: a looking glass for cancer? *Nat. Rev. Cancer* 12, 323–334. <https://doi.org/10.1038/nrc3261>.
- Mayekar, M.K., and Bivona, T.G. (2017). Current landscape of targeted therapy in lung cancer. *Clin. Pharmacol. Ther.* 102, 757–764. <https://doi.org/10.1002/cpt.810>.
- Mobadersany, P., Yousefi, S., Amgad, M., Gutman, D.A., Barnholtz-Sloan, J.S., Velázquez Vega, J.E., Brat, D.J., and Cooper, L.A.D. (2018). Predicting cancer outcomes from histology and genomics using convolutional networks. *Proc. Natl. Acad. Sci. USA* 115, E2970–E2979. <https://doi.org/10.1101/198010>.
- Cancer Genome Atlas Research Network (2013). Comprehensive molecular characterization of clear cell renal cell carcinoma. *Nature* 499, 43–49. <https://doi.org/10.1038/nature12222>.
- Nicholson, A.G., Perry, L.J., Cury, P.M., Jackson, P., McCormick, C.M., Corrin, B., and Wells, A.U. (2001). Reproducibility of the WHO/IASLC grading system for pre-invasive squamous lesions of the bronchus: a study of inter-observer and intra-observer variation. *Histopathology* 38, 202–208. <https://doi.org/10.1046/j.1365-2559.2001.01078.x>.
- Novara, G., Martignoni, G., Artibani, W., and Ficarra, V. (2007). Grading systems in renal cell carcinoma. *J. Urol.* 177, 430–436. <https://doi.org/10.1016/j.juro.2006.09.034>.
- Oh, J.H., Jang, S.J., Kim, J., Sohn, I., Lee, J.Y., Cho, E.J., Chun, S.M., and Sung, C.O. (2020). Spontaneous mutations in the single TTN gene represent high tumor mutation burden. *NPJ Genom. Med.* 5, 33–41. <https://doi.org/10.1038/s41525-019-0107-6>.
- Rabe, K., Snir, O.L., Bossuyt, V., Harigopal, M., Celli, R., and Reisenbichler, E.S. (2019). Interobserver variability in breast carcinoma grading results in prognostic stage differences. *Hum. Pathol.* 94, 51–57. <https://doi.org/10.1016/j.humpath.2019.09.006>.
- Rizvi, N.A., Hellmann, M.D., Snyder, A., Kvistborg, P., Makarov, V., Havel, J.J., Lee, W., Yuan, J., Wong, P., Ho, T.S., et al. (2015). Mutational landscape determines sensitivity to PD-1 blockade in non-small cell lung cancer. *Science* 348, 124–128. <https://doi.org/10.1126/science.aaa1348>.
- Saltz, J., Gupta, R., Hou, L., Kurc, T., Singh, P., Nguyen, V., Samaras, D., Shroyer, K.R., Zhao, T., Batiste, R., et al.; Cancer Genome Atlas Research Network (2018). Spatial organization and molecular correlation of tumor-infiltrating lymphocytes using deep learning on pathology images. *Cell Rep.* 23, 181–193.e7. <https://doi.org/10.1016/j.celrep.2018.03.086>.
- Schapiro, D., Jackson, H.W., Raghuraman, S., Fischer, J.R., Zanotelli, V.R.T., Schulz, D., Giesen, C., Catena, R., Varga, Z., and Bodenmiller, B. (2017). histoCAT: analysis of cell phenotypes and interactions in multiplex image cytometry data. *Nat. Methods* 14, 873–876. <https://doi.org/10.1038/nmeth.4391>.
- Shaban, M., Khurram, S.A., Fraz, M.M., Alsubaie, N., Masood, I., Mushtaq, S., Hassan, M., Loya, A., and Rajpoot, N.M. (2019). A novel digital score for abundance of tumour infiltrating lymphocytes predicts disease free survival in oral squamous cell carcinoma. *Sci. Rep.* 9, 13341–13413. <https://doi.org/10.1038/s41598-019-49710-z>.
- Shi, J.Y., Wang, X., Ding, G.Y., Dong, Z., Han, J., Guan, Z., Ma, L.J., Zheng, Y., Zhang, L., Yu, G.Z., et al. (2021). Exploring prognostic indicators in the pathological images of hepatocellular carcinoma based on deep learning. *Gut* 70, 951–961. <https://doi.org/10.1136/gutjnl-2020-320930>.
- Subramanian, A., Tamayo, P., Mootha, V.K., Mukherjee, S., Ebert, B.L., Gillette, M.A., Paulovich, A., Pomeroy, S.L., Golub, T.R., Lander, E.S., and Mesirov, J.P. (2005). Gene set enrichment analysis: a knowledge-based approach for interpreting genome-wide expression profiles. *Proc. Natl. Acad. Sci. USA* 102, 15545–15550. <https://doi.org/10.1073/pnas.0506580102>.
- Sundararajan, M., Taly, A., and Yan, Q. (2017). July. Axiomatic attribution for deep networks. In International conference on machine learning, pp. 3319–3328.
- Tarantino, P., Mazzarella, L., Marra, A., Trapani, D., and Caviglino, G. (2021). The evolving paradigm of biomarker actionability: histology-agnosticism as a spectrum, rather than a binary quality. *Cancer Treat Rev.* 94, 102169. <https://doi.org/10.1016/j.ctrv.2021.102169>.
- Thorsson, V., Gibbs, D.L., Brown, S.D., Wolf, D., Bortone, D.S., Ou Yang, T.H., Porta-Pardo, E., Gao, G.F., Plaisier, C.L., Eddy, J.A., et al. (2018). The immune landscape of cancer. *Immunity* 48, 812–830.e14. <https://doi.org/10.1016/j.imuni.2021.01.011>.
- Tsamardinos, I., Greasidou, E., and Borboudakis, G. (2018). Bootstrapping the out-of-sample predictions for efficient and accurate cross-validation. *Mach. Learn.* 107, 1895–1922. <https://doi.org/10.1007/s10994-018-5714-4>.
- Uhlen, M., Karlsson, M.J., Zhong, W., Tebani, A., Pou, C., Mikes, J., Lakshmikanth, T., Forsström, B., Edfors, F., Odeberg, J., et al. (2019). A genome-wide transcriptomic analysis of protein-coding genes in human

- blood cells. *Science* 366, eaax9198. <https://doi.org/10.1126/science.aax9198>.
- Uhlen, M., Zhang, C., Lee, S., Sjöstedt, E., Fagerberg, L., Bidkori, G., Benfeitas, R., Arif, M., Liu, Z., Edfors, F., et al. (2017). A pathology atlas of the human cancer transcriptome. *Science* 357, eaan2507. <https://doi.org/10.1126/science.aan2507>.
- Uhlén, M., Fagerberg, L., Hallström, B.M., Lindskog, C., Oksvold, P., Mardinoglu, A., Sivertsson, Å., Kampf, C., Sjöstedt, E., Asplund, A., et al. (2015). Tissue-based map of the human proteome. *Science* 347, 1260419. <https://doi.org/10.1126/science.1260419>.
- Vale-Silva, L.A., and Rohr, K. (2021). Long-term cancer survival prediction using multimodal deep learning. *Sci Rep* 11, 13505. <https://doi.org/10.1038/s41598-021-92799-4>.
- Wang, W., Tran, D., and Feiszli, M. (2020). What makes training multi-modal classification networks hard? In Proceedings of the IEEE/CVF Conference on Computer Vision and Pattern Recognition, pp. 12695–12705. <https://doi.org/10.1109/cvpr42600.2020.01271>.
- Wulczyn, E., Steiner, D.F., Xu, Z., Sadhwani, A., Wang, H., Flament-Auvigne, I., Mermel, C.H., Chen, P.C., Liu, Y., and Stumpe, M.C. (2020). Deep learning-based survival prediction for multiple cancer types using histopathology images. *PLoS One* 15, e0233678. <https://doi.org/10.1371/journal.pone.0233678>.
- Wulczyn, E., Steiner, D.F., Moran, M., Plass, M., Reihs, R., Tan, F., Flament-Auvigne, I., Brown, T., Regitnig, P., Chen, P.C., et al. (2021). Interpretable survival prediction for colorectal cancer using deep learning. *NPJ Digit. Med.* 4, 71. <https://doi.org/10.1038/s41746-021-00427-2>.
- Zadeh, A., Chen, M., Poria, S., Cambria, E., and Morency, L.-P. (2017). Tensor Fusion Network for Multimodal Sentiment Analysis (Association for Computational Linguistics). <https://doi.org/10.18653/v1/D17-1115>.
- Zadeh, S.G., and Schmid, M. (2021). Bias in cross-entropy-based training of deep survival networks. *IEEE Trans. Pattern Anal. Mach. Intell.* 43, 3126–3137. <https://doi.org/10.1109/tpami.2020.2979450>.
- Zhou, Q., Xu, C.R., Cheng, Y., Liu, Y.P., Chen, G.Y., Cui, J.W., Yang, N., Song, Y., Li, X.L., Lu, S., et al. (2021). Bevacizumab plus erlotinib in Chinese patients with untreated, EGFR-mutated, advanced NSCLC (ARTEMIS-CTONG1509): a multicenter phase 3 study. *Cancer Cell* 39, 1279–1291.e3. <https://doi.org/10.1016/j.ccr.2021.07.005>.

STAR★METHODS

KEY RESOURCES TABLE

REAGENT or RESOURCE	SOURCE	IDENTIFIER
Biological samples		
Whole slide images (TCGA)	https://portal.gdc.cancer.gov/	RRID:SCR_003193
Deposited data		
The Cancer Genome Atlas	https://portal.gdc.cancer.gov/	RRID:SCR_003193
Software and algorithms		
PORPOISE	This paper; https://github.com/mahmoodlab/PORPOISE	
CLAM	https://github.com/mahmoodlab/CLAM	
Pathomic Fusion	https://github.com/mahmoodlab/PathomicFusion	
HoVeR-Net	https://github.com/vqdang/hover_net	
Python (3.7.7)	https://www.python.org/	RRID:SCR_008394
NVIDIA CUDA (11.0)	https://developer.nvidia.com/cuda-toolkit	
NVIDIA cuDNN (7.5)	https://developer.nvidia.com/cudnn	
PyTorch (1.6.0)	https://pytorch.org	RRID:SCR_018536
Captum (0.2.0)	https://captum.ai	
NumPy (1.18.1)	http://www.numpy.org	RRID:SCR_008633
Pandas (1.1.3)	https://pandas.pydata.org	RRID:SCR_018214
PIL (7.0.0)	https://pillow.readthedocs.io/en/stable/	
Openslide (1.1.1)	https://openslide.org/	
Scipy (1.4.1)	http://www.scipy.org	RRID:SCR_008058
Lifelines (0.24.6)	https://lifelines.readthedocs.io/	
Seaborn (0.9.0)	https://seaborn.pydata.org/	
Matplotlib (3.1.1)	https://matplotlib.org/	RRID:SCR_008624
Shap (0.35.0)	https://shap.readthedocs.io/en/latest/index.html	

RESOURCE AVAILABILITY

Lead contact

Further information and requests regarding this manuscript should be sent to and will be fulfilled by the lead investigator, Faisal Mahmood (faisalmahmood@bwh.harvard.edu).

Materials availability

This study did not generate any unique reagents.

Data and code availability

All diagnostic whole slide images (WSIs) and their corresponding molecular and clinical data were obtained from The Cancer Genome Atlas and are publicly accessible through the NIH Genomic Data Commons Data Portal <https://portal.gdc.cancer.gov/>. All code was implemented in Python, using PyTorch as the primary deep learning package. All code and scripts to reproduce the experiments of this paper are available at: <https://github.com/mahmoodlab/PORPOISE>.

METHOD DETAILS

Dataset description

6,592 H&E diagnostic WSIs with corresponding molecular and clinical data were collected from 5,720 patients across 14 cancer types from TCGA via the NIH Genomic Data Commons Data Portal. Sample inclusion criteria in dataset collection were

defined by: 1) dataset size and distribution of uncensored-to-censored patients in each TCGA project, and 2) availability of matching CNV, mutation, and RNA-Seq abundances for each WSI (WSI-CNV-MUT-RNA). To mitigate overfitting in modeling the survival distribution during survival analysis, TCGA projects with less than 150 patients (after WSI and molecular data alignment) and have poor uncensorship (less than 5% uncensored patients) were excluded from the study. For the gastrointestinal tract, cancer types from these organs were grouped together respectively, forming the combined TCGA project - COADREAD (colon (COAD) and rectal (READ) adenocarcinoma). For LGG, other cases in the TCGA glioma cohort (such as glioblastomas) were included during model training, with evaluation and interpretability only performed on LGG cases. For inclusion of Skin Cutaneous Melanoma (TCGA-SKCM) and Uterine Corpus Endometrial Carcinoma (TCGA-UCEC) that have large data missingness, criteria for data alignment were relaxed to include samples with only matching WSI-MUT-RNA and WSI-CNV-MUT respectively. We note that in TCGA-SKCM, we also included metastatic cases as very few primary tumors had matching molecular profile information. To decrease feature sparsity in molecular profile data, genes with greater than 10% CNV or 5% mutation frequency in each cancer study were used. In TCGA-SKCM and TCGA-UCEC, we used mutation frequency cutoffs of 10%, as using the cutoff for other cancer types resulted in few-to-zero gene features. To limit the number of the features from RNA-Seq, we used gene sets from the gene family categories from the Molecular Signatures Database ([Subramanian et al., 2005](#)). Molecular and clinical data were obtained from quality-controlled files from the cBioPortal. Summary tables of cohort characteristics, censorship statistics, and feature alignment can be found in [Tables S1](#) and [S3](#).

WSI processing

For each WSI, automated segmentation of tissue was performed using the public CLAM ([Lu et al., 2021](#)) repository for WSI analysis. Following segmentation, image patches of size 256×256 were extracted without overlap at the $20 \times$ equivalent pyramid level from all tissue regions identified. Subsequently, a ResNet50 model pretrained on ImageNet is used as an encoder to convert each 256×256 patch into 1024-dimensional feature vector, via spatial average pooling after the 3rd residual block. To speed up this process, multiple GPUs were used to perform computation in parallel using a batch-size of 128 per GPU.

Deep learning-based survival analysis for integrating whole slide images and genomic features

PORPOISE (Pathology-Omics Research Platform for Integrated Survival Estimation) uses a high-throughput, interpretable, weakly-supervised, multimodal deep learning algorithm (MMF) designed for integrating whole slide images and molecular profile data in weakly-supervised learning tasks such as patient-level cancer prognosis via survival analysis. Given 1) diagnostic WSIs as pyramidal files and 2) processed genomic and transcriptomic features for a single patient, MMF learns to jointly represent these two heterogeneous data modalities. Though tasked for survival analysis, our algorithm is adaptable to any combination of modalities, and flexible for solving any learning tasks in computational pathology that have patient-level labels. Our algorithm consists of three components: 1) attention-based Multiple Instance Learning (AMIL) for processing WSIs, 2) Self-Normalizing Networks (SNN) for processing molecular profile data, and 3) a multimodal fusion layer (extended from Pathomic Fusion) for integrating WSIs and molecular profile data ([Chen et al., 2020](#); [Ilse et al., 2018](#); [Klambauer et al., 2017](#); [Lu et al., 2021](#)).

AMIL

To perform survival prediction from WSIs, we extend the attention-based multiple instance learning algorithm, which was originally proposed for weakly-supervised classification. Under the multiple instance learning framework, each gigapixel WSI is divided into smaller regions and viewed as a collection (bag) of patches (instances) with a corresponding slide-level label used for training. Accordingly, following WSI processing, each WSI bag is represented by a $M_i \times C$ matrix tensor, where M_i is the number of patches (bag size), which varies between slides, and C is the feature dimension and equals 1024 for the ResNet50 encoder we used. Since survival outcome information is available at the patient-level instead of for individual slides, we collectively treat all WSIs corresponding to a patient case as a single WSI bag during training and evaluation. Namely, for a patient case with N WSIs with bag sizes M_1, \dots, M_N respectively, the WSI bag corresponding the patient is formed by concatenating all N bags, and has dimensions $M \times 1024$, where $M = \sum_{i=1}^N M_i$.

The model can be described by three components, the projection layer f_p , the attention module f_{attn} , and the prediction layer f_{pred} . Incoming patch-level embeddings of each WSI bag, $\mathbf{H} \in \mathbb{R}^{M \times 1024}$, are first mapped into a more compact, dataset-specific 512-dimensional feature space by the fully-connected layer f_p with weights $\mathbf{W}_{proj} \in \mathbb{R}^{512 \times 1024}$ and bias $\mathbf{b}_{bias} \in \mathbb{R}^{512}$. For succinctness, from now on, we refer to layers using their weights only (the bias terms are implied). Subsequently, the attention module f_{attn} learns to score each region for its perceived relevance to patient-level prognostic prediction. Regions with high attention scores contribute more to the patient-level feature representation relative to regions assigned low attention scores, when information across all regions in the patient's WSIs are aggregated, in an operation known as attention-pooling ([Ilse et al., 2018](#)). Specifically, f_{attn} consists of 3 fully-connected layers with weights $\mathbf{U}_a \in \mathbb{R}^{256 \times 512}$, $\mathbf{V}_a \in \mathbb{R}^{256 \times 512}$ and $\mathbf{W}_a \in \mathbb{R}^{1 \times 256}$. Given a patch embedding $\mathbf{h}_m \in \mathbb{R}^{512}$ (the m^{th} row entry of \mathbf{H}), its attention score a_m is computed by:

$$a_m = \frac{\exp\{\mathbf{W}_a(\tanh(\mathbf{V}_a \mathbf{h}_m^\top) \odot \text{sigm}(\mathbf{U}_a \mathbf{h}_m^\top))\}}{\sum_{m=1}^M \exp\{\mathbf{W}_a(\tanh(\mathbf{V}_a \mathbf{h}_m^\top) \odot \text{sigm}(\mathbf{U}_a \mathbf{h}_m^\top))\}}$$

The attention-pooling operation then aggregates the patch-level feature representations into the patient representation $\mathbf{h}_{\text{patient}} \in \mathbb{R}^{512}$ using computed attention scores as weight coefficients, where $\mathbf{A} \in \mathbb{R}^M$ is the vector of attention scores:

$$\mathbf{h}_{\text{patient}} = \text{Attnpool}(\mathbf{A}, \mathbf{H}) = \sum_{m=1}^M a_m \mathbf{h}_m$$

The final patient-level prediction scores \mathbf{s} are computed from the bag representation using the prediction layer f_{pred} with weights $\mathbf{W}_{\text{pred}} \in \mathbb{R}^{4 \times 512}$ and sigmoid activation: $\mathbf{s} = f_{\text{pred}}(\mathbf{h}_{\text{bag}})$. This architectural choice and the negative-log-likelihood function for discrete-time survival modeling, are described in detail in a proceeding section. The last fully-connected layer is used to learn a representation $\mathbf{h}_{\text{WSI}} \in \mathbb{R}^{32 \times 1}$, which is then used as input to our multimodal fusion layer.

SNN

For survival prediction using molecular features, we used the Self-Normalizing Network (SNN) which has previously been demonstrated to work well in high-dimensional low-sample size (HDLSS) scenarios (Klambauer et al., 2017). For learning scenarios such as genomics that have hundreds to thousands of features with relatively few training samples, traditional Feedforward networks are prone to overfitting, as well as training instabilities from current deep learning regularization techniques such as stochastic gradient descent and Dropout. To employ more robust regularization techniques on high-dimensional low sample size genomics data, we adopted the normalizing activation and dropout layers from the SNN architecture: 1) scaled exponential linear units (SeLU) and 2) Alpha Dropout. In comparison with rectified linear unit (ReLU) activations common in current Feedforward networks, SeLU activations would drive the outputs of every layer toward zero mean and unit variance during layer propagation. The SeLU activation is defined as:

$$\text{SeLU}(x) = \lambda \begin{cases} x & \text{if } x > 0 \\ \alpha e^x - \alpha & \text{if } x \leq 0 \end{cases}$$

where $\alpha \approx 1.67, \lambda \approx 1.05$. To main normalization after Dropout, instead of setting the activation value to be 0 with probability $1 - q$ for $0 < q \geq 1$ for a neuron in a given layer, the activation value is set to be $\lim_{x \rightarrow -\infty} \text{SeLU}(x) = -\lambda\alpha = \alpha'$, which ensures the self-normalization property with updated mean and variance:

$$\mathbb{E}(xd + \alpha'(1 - d)) = q\mu + (1 - q)\alpha', \quad \text{Var}(xd + \alpha'(1 - d)) = q((1 - q)(\alpha' - \mu)^2 + \nu).$$

The SNN architecture used for molecular feature input consists of 2 hidden layers of 256 neurons each, with SeLU activation and Alpha Dropout applied to every layer. The last fully-connected layer is used to learn a representation $\mathbf{h}_{\text{molecular}} \in \mathbb{R}^{32 \times 1}$, which is then used as input to our multimodal fusion layer. We ablated performance of MMF using fully-connected layers without self-normalization and also without \mathcal{L}_1 regularization, and found that self-normalization and \mathcal{L}_1 regularization are important for multimodal training (Tables S3 and S3)

Multimodal fusion layer

Following the construction of unimodal feature representations from the AMIL and SNN subnetworks, we learn a multimodal feature representation using Kronecker Product Fusion, which would capture important interactions between these two modalities (Chen et al., 2020; Zadeh et al., 2017). Our joint multimodal tensor is computed by the Kronecker product of \mathbf{h}_{WSI} and $\mathbf{h}_{\text{molecular}}$, in which every neuron in $\mathbf{h}_{\text{molecular}}$ is multiplied by every other neuron in \mathbf{h}_{WSI} to capture all bimodal interactions. To also preserve the unimodal features, we also append "1" to each unimodal feature representation before fusion, which is shown the equation below:

$$\mathbf{h}_{\text{fusion}} = \begin{bmatrix} \mathbf{h}_{\text{WSI}} \\ 1 \end{bmatrix} \otimes \begin{bmatrix} \mathbf{h}_{\text{molecular}} \\ 1 \end{bmatrix}$$

where \otimes is the Kronecker Product, and $\mathbf{h}_{\text{fusion}} \in \mathbb{R}^{33 \times 33}$ is a differentiable multimodal tensor that models all unimodal and biomodal interaction with $O(1)$ computation. To decrease impact of noise unimodal features and to reduce feature collinearity between the WSI and molecular feature modalities, we used a gating-based attention mechanism that additionally controls the expressiveness of each modality:

$$\begin{aligned} \mathbf{h}_{i,\text{gated}} &= \mathbf{z}_i * \mathbf{h}_i, \quad \forall h_i \in \{\mathbf{h}_{\text{WSI}}, \mathbf{h}_{\text{molecular}}\} \\ \text{where, } \mathbf{h}_i &= \text{ReLU}(\mathbf{W}_i \cdot \mathbf{h}_i) \\ \mathbf{z}_i &= \sigma(\mathbf{W}_j \cdot [\mathbf{h}_{\text{WSI}}, \mathbf{h}_{\text{molecular}}]) \end{aligned}$$

For a modality i with learned unimodal features h_i , we learn a weight matrix \mathbf{W}_i that would score the relative importance of each feature in modality i . After performing Softmax, \mathbf{z}_i can be interpreted as an attention score of how \mathbf{h}_{WSI} and $\mathbf{h}_{\text{molecular}}$ attends to each feature in h_i . We obtain the gated representation $\mathbf{h}_{i,\text{gated}}$ in taking the element-wise product of the original unimodal features h_i and attention scores \mathbf{z}_i . In our implementation of gating-based attention, we applied gating to both modalities prior to fusion, with additional skip connections made to the penultimate hidden layer of our multimodal network. Following Kronecker Product Fusion, we propagate our multimodal tensor through two hidden layers of size 256, which is then subsequently supervised using a cross entropy-based loss function for survival analysis. Table S3 shows an ablation study in using multimodal gating for pathology gating only, genomic gating only, and both pathology and genomic gating prior to Kronecker Product Fusion. To assess multimodal

performance with other fusion mechanisms, we compared vector concatenation and a low-rank implementation of Kronecker Product Fusion, which similarly outperform unimodal approaches (Table S3) (Liu et al., 2018).

Survival loss function

To perform survival prediction from right-censored, patient-level survival data, we first partition the continuous timescale of overall patient survival time in months, T_{cont} into 4 non-overlapping bins: $[t_0, t_1), [t_1, t_2), [t_2, t_3), [t_3, t_4)$, where $t_0 = 0$, $t_4 = \infty$ and t_1, t_2, t_3 define the quartiles of event times for uncensored patients. Subsequently, for each patient entry in the dataset, indexed by j with corresponding follow-up time $T_{j,cont} \in [0, \infty)$, we define the discretized event time T_j as the index of the bin interval that contains $T_{j,cont}$:

$$T_j = r \text{ iff } T_{j,cont} \in [t_r, t_{r+1})$$

To avoid confusion, we refer to the discretized ground truth label of the j^{th} patient as Y_j . For a given patient with bag-level representation \mathbf{h}_{bag_j} , the prediction layer f_{pred} with weights $\mathbf{W}_{pred} \in \mathbb{R}^{4 \times 512}$ models the hazard function defined as:

$$f_{hazard}(r | \mathbf{h}_{bag_j}) = P(T_j = r | T_j \geq r, \mathbf{h}_{bag_j})$$

which relates to the survival function through:

$$\begin{aligned} f_{surv}(r | \mathbf{h}_{bag_j}) &= P(T_j > r | \mathbf{h}_{bag_j}) \\ &= \prod_{u=1}^r (1 - f_{hazard}(u | \mathbf{h}_{bag_j})) \end{aligned}$$

To optimize the model parameters, we use the log likelihood function for a discrete survival model (Zadeh and Schmid, 2020), which given the binary censorship status c_j , can be expressed as

$$\begin{aligned} L = -I &= -c_j \cdot \log(f_{surv}(Y_j | \mathbf{h}_{bag_j})) \\ &\quad - (1 - c_j) \cdot \log(f_{surv}(Y_j - 1 | \mathbf{h}_{bag_j})) \\ &\quad - (1 - c_j) \cdot \log(f_{hazard}(Y_j | \mathbf{h}_{bag_j})) \end{aligned}$$

In this formulation, we use $c_j = 1$ for patients who have lived past the end of the follow-up period and $c_j = 0$ in the event that the patient passed away precisely at time $T_{j,cont}$. During training, the contribution of uncensored patient cases can be emphasized by minimizing a weighted sum of L and $L_{uncensored}$

$$L_{surv} = (1 - \beta) \cdot L + \beta \cdot L_{uncensored}$$

The second term of the loss function corresponding uncensored patients, is defined by:

$$\begin{aligned} L_{uncensored} &= -(1 - c_j) \cdot \log(f_{surv}(Y_j - 1 | \mathbf{h}_{bag_j})) \\ &\quad - (1 - c_j) \cdot \log(f_{hazard}(Y_j | \mathbf{h}_{bag_j})) \end{aligned}$$

Training details

For each disease model studied patient cases were randomly split into non-overlapping training (80%) and test (20%) sets that were used to train models and evaluate the performance. These training and test sets were constructed at a patient case level i.e., all slides corresponding to a given patient case were only present in either the test or train set and slides from the same case were never simultaneously part of training and testing. We repeated the experiments for each disease model in a five-fold cross-validation reassigning patient cases into non-overlapping training and testing cohorts five times. The same procedure was adopted for training and evaluating MMF and unimodal models. Across all cancer types, MMF is trained end-to-end with AMIL subnetwork, SNN subnetwork and multimodal fusion layer, using Adam optimization with a learning rate of 2×10^{-4} , b_1 coefficient of 0.9, b_2 coefficient of 0.999, \mathcal{L}_2 weight decay of 1×10^{-5} , and \mathcal{L}_1 weight decay of 1×10^{-5} for 20 epochs. Because WSIs across patient samples have varying image dimension sizes, we randomly sampled paired WSIs and molecular features with a mini-batch size of 1. In performing comparative analyses with unimodal networks, AMIL and SNN were also trained independently using the same survival loss function and hyperparameters as MMF.

Multimodal interpretability and visualization

Local WSI Interpretability. For a given WSI, to perform visual interpretation of the relative importance of different tissue regions toward the patient-level prognostic prediction, we first compute attention scores for 256×256 patches (without overlap) from all tissue regions in the slide. We refer to the attention score distribution across all patches from all WSIs from the patient case as the reference distribution. For fine-grained attention heatmaps, attention scores for each WSI are recomputed by increasing the tiling overlap to up to 90%. For visualization, the attention scores are converted to percentile scores between 0.0 (low attention) to 1.0 (high attention) using the initial reference distribution, and spatially registered onto the corresponding WSIs (scores from overlapping patches are

averaged). The resulting heatmap, referred to as local WSI interpretability, is transformed to RGB values using a colormap and overlaid onto the original H&E image with a transparency value of 0.5. To interpret these heatmaps, note that in contrast with classification tasks in which attention heatmaps would localize areas of diagnostic relevance for predicting a discrete class, survival outcome prediction is an ordinal regression task in which high attention weights correspond to regions with high prognostic relevance in determining relative predicted risk. For example, WSIs with predicted high-risk scores would have high attention on high tumor grade or tumor invasion regions used in explaining poor survival, whereas WSIs with predicted low risk scores would have high attention on low tumor grade or lymphocyte-containing regions used in explaining favorable survival.

Global WSI interpretability

For sets of WSIs belonging to different patient cohorts, we performed global WSI interpretability by quantifying and characterizing the morphological patterns in the highest-attended image patches from each WSI. Since WSIs have differing image dimensions, we extracted a proportional amount of high attention image patches (1%) to the total image dimension. On average, each WSI contained 13,487 512×512 40× images, with approximately 135 image patches used as high attention regions. These attention patches are analyzed using a HoverNet model pretrained for simultaneous cell instance segmentation and classification (Graham et al., 2019). Cells are classified as either tumor cells (red), lymphocytes (green), connective tissue (blue), dead cells (yellow), or non-neoplastic epithelial cells (orange). For each of these cell types, we analyzed the cell type frequency across all counted cells in the highest-attended image patches in a given patient, then analyzed the cell fraction distribution across all patients in low-risk and high-risk patients, defined as patients below and above the 25% and 75% predicted risk percentiles respectively.

Tumor-Infiltrating Lymphocyte detection

To detect Tumor-Infiltrating Lymphocyte (TIL) presence in image patches, similar to other work, we defined TIL presence as the co-localization of tumor and immune cells which reflects intratumoral TIL response (Maley et al., 2015; Shaban et al., 2019). Following cell instance segmentation and classification of tumor and immune cells in the highest-attended 512×512 20× image patches, we defined a heuristic which classified an image patch as positive for TIL presence with high tumor-immune cell co-localization (patch containing more than 20 counted cells, and more than 10 detected lymphocytes and 5 detected tumor cells). Similar to computing cell fraction distributions, for the highest-attended image patches in a given patient, we computed the fraction of TIL positive image patches, and plotted its distribution in low and high risk patients.

Local and global SNN interpretability

For a given set of molecular features x belonging to a patient sample, to characterize feature importance magnitude and direction of impact, we used Integrated Gradients (IG), a gradient-based feature attribution method that attributes the prediction of deep networks to their inputs (Sundararajan et al., 2017). IG satisfies two axioms for interpretability: 1) Sensitivity, in which for every desired input x and baseline x_i that differ in one feature but have different predictions, the differing feature should be given a non-zero attribution, and 2) Implementation Invariance, which states that two networks are functionally equivalent if their outputs are equal for all inputs. For a given input x , IG calculates the gradients of x across different scales against a zero-scaled baseline x_i , which then uses the Gauss-Legendre quadrature to approximate the integral of gradients.

$$IG_i(x) ::= (x_i - x'_i) \times \int_{\alpha=0}^1 \frac{\partial F(x' + \alpha \times (x - x'))}{\partial x_i} d\alpha$$

Using IG, for each molecular feature in input x belonging to a patient sample, we compute feature attribution values, which corresponds to the magnitude of how much varying that feature in x will change the output. Features that have no impact on the output would have zero attribution, whereas features that affect the output would have larger magnitude (interpreted as feature importance). In the context of regression tasks such as survival analysis, features that are positive attribution contribute toward increasing the output value (high risk), whereas negative attribution corresponds with decreasing the output value (low risk). For individual samples, we can use IG to understand how molecular features contribute toward the model risk prediction, which we can visualize as bar plots (termed local interpretability), where the x axis corresponds with attribution value, the y axis ranks features in order of absolute attribution magnitude (in descending order), and color corresponds with feature value. For binary data such as mutation status, bar colors are either colored blue (feature value '0', wildtype) or red (feature value '1', or mutation). For categorical and continuous data such as copy number variation and RNA-Seq abundance, bar colors are visualized using heatmap colors, where blue is low feature value (copy number loss/low RNA-Seq abundance) and red is high feature value (copy number gain/high RNA-Seq abundance). For large cohorts of patients from a cancer type, we can visualize the distribution of feature attributions across all patients (termed global interpretability), where each dot represents the attribution and feature value of an individual feature of an individual patient sample. Plots and terminology for local and global interpretability were derived from decision plots in Shapley Additive Explanation-based methods (Lundberg et al., 2020).

Measuring WSI contribution in model prediction

To measure the contribution of WSIs in model predictions, for each patient sample, we compute the attributions for each modality at the penultimate hidden layer before multimodal fusion (last layer of the SNN and AMIL subnetworks). Then, we normalize the sum of absolute attribution values for each modality, to estimate percentage that each modality contributes toward the model prediction (Kokhlikyan et al., 2020).

Computational hardware and software

PORPOISE was built with the OpenSeaDragon API and is hosted on Google Cloud. Python (version 3.7.7) packages used by PORPOISE include PyTorch (version 1.3.0), Lifelines (version 0.24.6), NumPy (version 1.18.1), Pandas (version 1.1.3), PIL (version 7.0.0), and OpenSlide (version 1.1.1). All WSIs were processed on Intel Xeon multi-core CPUs (Central Processing Units) and a total of 16 2080 Ti GPUs (Graphics Processing Units) using our custom, publicly available CLAM ([Lu et al., 2021](#)) whole slide processing pipeline. The multimodal fusion layer for integrating WSIs and molecular profiles was implemented using our custom, publicly available Pathomic Fusion ([Chen et al., 2020](#)) software implemented in Python. Deep learning models were trained with Nvidia softwares CUDA 11.0 and cuDNN 7.5. Integrated Gradients was implemented using Captum (version 0.2.0) ([Kokhlikyan et al., 2020](#)). Cell instance segmentation and classification was implemented using the HoVerNet software ([Graham et al., 2019](#)). Statistical analyses such as two-sampled t-tests and log -rank tests used implementations from SciPy (1.4.1) and Lifelines (version 0.24.6) respectively. Plotting and visualization packages were generated using Seaborn (0.9.0), Matplotlib (version 3.1.1), and Shap (0.35.0).

QUANTIFICATION AND STATISTICAL ANALYSIS

To plot the Kaplan-Meier curves, we aggregated out-of-sample risk predictions from the validation folds and plotted them against their survival time ([Mobadersany et al., 2018](#)). For significance testing of patient stratification in Kaplan-Meier analysis, we use the log -rank test to measure if the difference of two survival distributions is statistically significant (P-Value < 0.05) ([Bland and Altman, 2004](#)). Cross-validated c-Index performance is reported as the average c-Index over the 5-folds. To estimate 95% confidence intervals in cross-validation, we performed non-parametric bootstrapping using 1000 replicates on the out-of-sample predictions in the validation folds ([LeDell et al., 2015](#); [Tsamardinos et al., 2018](#)). In addition to c-Index, we also report Cumulative/Dynamic AUC (termed Survival AUC), a time-dependent measure of model performance that evaluates how well the model stratifies patient risk across various time points, and additionally corrects for optimistic bias from censorship via computing an inverse probability of censor weighting. For assessing global morphological feature significance of individual cell type presence, two-sample t-tests were performed in evaluating the statistical significance of mean cell fraction distributions in the top 1% of high attention regions of low and high-risk patients (P-Value < 0.05). For assessing global molecular feature significance of individual gene features, two-sample t-tests were performed in evaluating the statistical significance of attribution distributions of low and high gene feature values (below and above median gene feature value respectively). For all boxplots, boxes indicate the 1st, median, and 3rd quartile values of the data distribution, and whiskers extend to data points within $1.5 \times$ the interquartile range.

Supplemental information

**Pan-cancer integrative histology-genomic
analysis via multimodal deep learning**

Richard J. Chen, Ming Y. Lu, Drew F.K. Williamson, Tiffany Y. Chen, Jana Lipkova, Zahra Noor, Muhammad Shaban, Maha Shady, Mane Williams, Bumjin Joo, and Faisal Mahmood

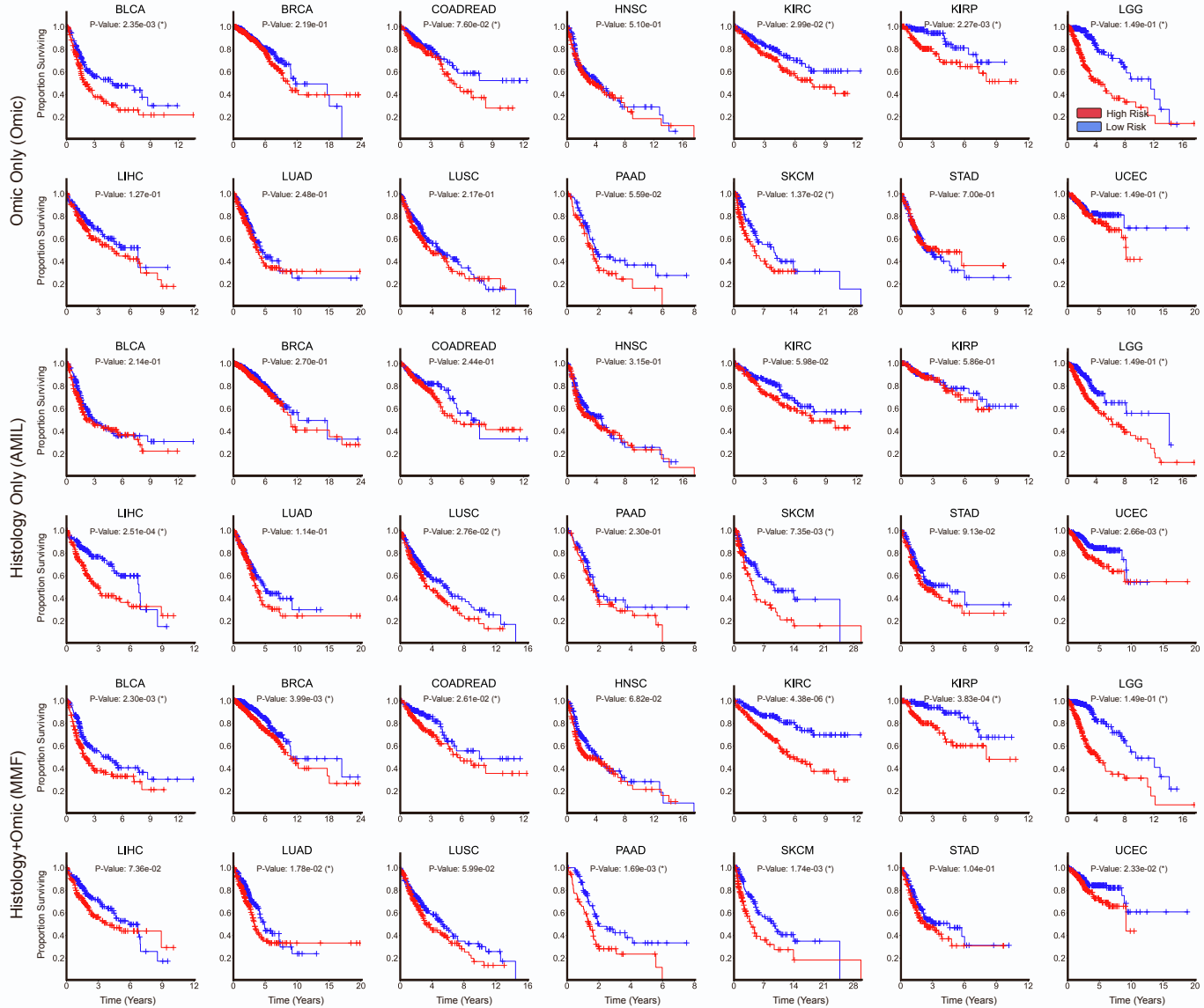


Figure S1: Kaplan-Meier comparative analysis of SNN, AMIL, and MMF. Related to Figure 2A. Kaplan-Meier comparative analysis of SNN, AMIL, and MMF of patient stratification of low- and high-risk patients across all 14 cancer types. Low- and high-risks are defined by the median 50% percentile of risk predictions. Logrank test was used to test for statistical significance in survival distributions between low- and high-risk patients (with * marked if P-Value < 0.05). For all model types and cancer types, out-of-sample risk predictions in the validation folds were pooled to show overall survival distribution on the entire cohort.

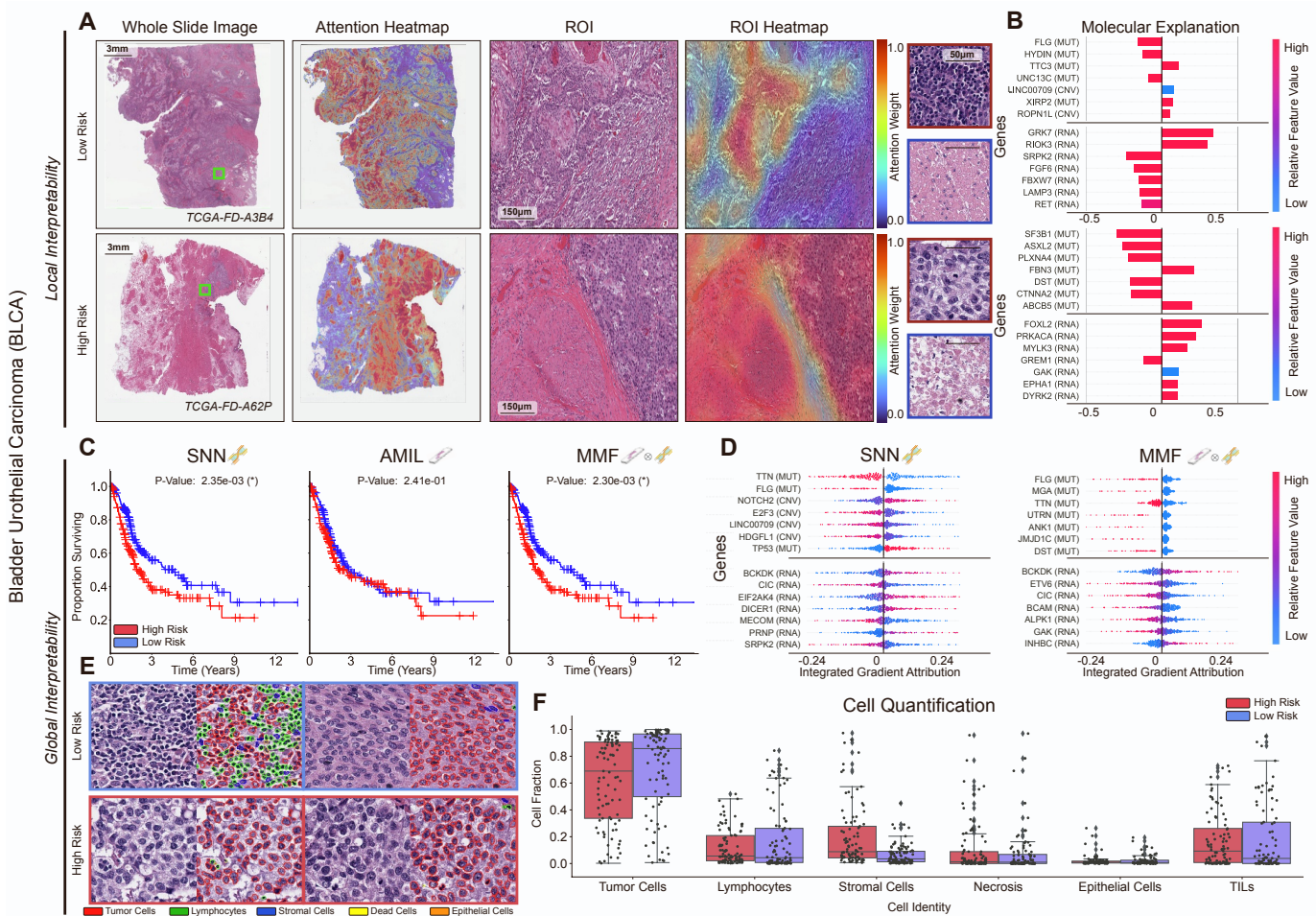


Figure S2: Quantitative performance, local model explanation, and global interpretability pooled analyses of PORPOISE on BLCA. Related to Figure 3, 4, 5, and 6. **A.** WSIs, associated attention heatmaps, ROIs, ROI heatmaps, and selected high attention patches from example low-risk (top) and high-risk (bottom) cases. In BLCA ($n=358$), high attention for low-risk cases ($n=90$) tends to focus on aggregates of lymphocytes, thick tumor papillae, and muscularis, while in high-risk cases ($n=93$), high attention focuses on sheet-like and solid tumor growth, muscularis, and areas of necrosis. **B.** Local gene attributions for the corresponding low-risk (top) and high-risk (bottom) cases. **C.** Kaplan–Meier curves for omics-only (left, "SNN"), histology-only (center, "AMIL") and multimodal fusion (right, "MMF"), showing improved patient stratification over AMIL and long-surviving patients in SNN. Logrank test was used to test for statistical significance in survival distributions between low- and high-risk patients (with * marked if $P\text{-Value} < 0.05$). **D.** Global gene attributions across patient cohorts according to unimodal interpretability (left, "SNN"), and multimodal interpretability (right, "MMF"). **E.** High attention patches from low-risk (top) and high-risk (bottom) cases with corresponding cell labels. **F.** Quantification of cell types in high attention patches for all cases of BLCA with high-risk in red and low-risk in blue, showing high tumor cell abundance in both risk groups, with increased stromal cell presence in high-risk groups. Boxes indicate quartile values and whiskers extend to data points within $1.5 \times$ the interquartile range.

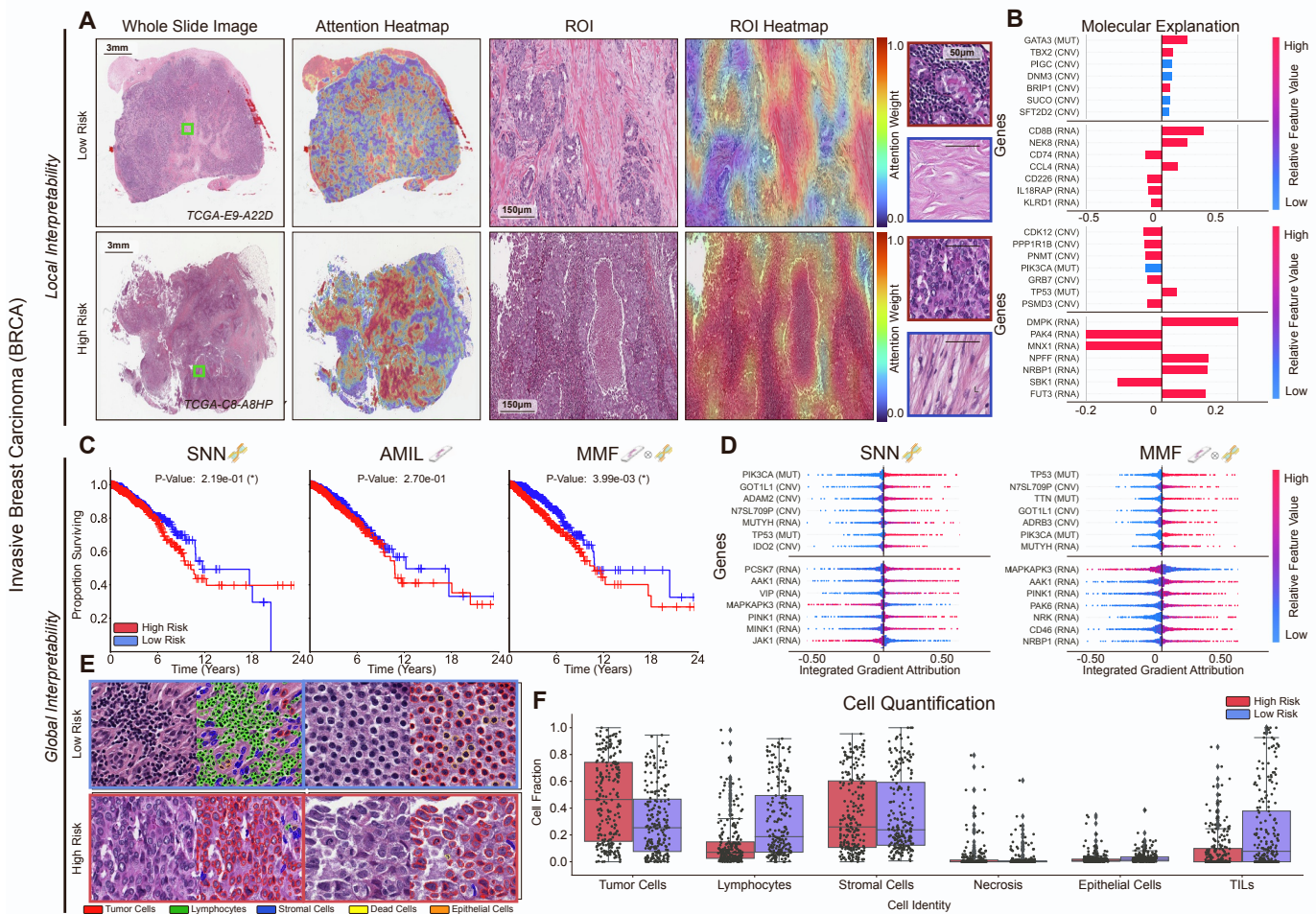


Figure S3: Quantitative performance, local model explanation, and global interpretability analyses of PORPOISE on BRCA. Related to Figure 3, 4, 5, and 6. **A.** WSIs, associated attention heatmaps, ROIs, ROI heatmaps, and selected high attention patches from example low-risk (top) and high-risk (bottom) cases. In BRCA (n=730), high attention for low-risk cases (n=22) tends to focus on collagenous stroma and aggregates of lymphocytes, while in high-risk cases (n=223), high attention focuses on areas of tumor cells with increased mitotic activity, nuclear pleomorphism, and necrosis. **B.** Local gene attributions for the corresponding low-risk (top) and high-risk (bottom) cases. **C.** Kaplan–Meier curves for omics-only (left, "SNN"), histology-only (center, "AMIL") and multimodal fusion (right, "MMF"), showing improved patient stratification over AMIL and long-surviving patients in SNN. Logrank test was used to test for statistical significance in survival distributions between low- and high-risk patients (with * marked if P-Value < 0.05). **D.** Global gene attributions across patient cohorts according to unimodal interpretability (left, "SNN"), and multimodal interpretability (right, "MMF"). **E.** High attention patches from low-risk (top) and high-risk (bottom) cases with corresponding cell labels. **F.** Quantification of cell types in high attention patches for each disease overall, showing decreased tumor cell abundance and increased lymphocyte and TIL presence in low-risk groups. Boxes indicate quartile values and whiskers extend to data points within $1.5 \times$ the interquartile range.

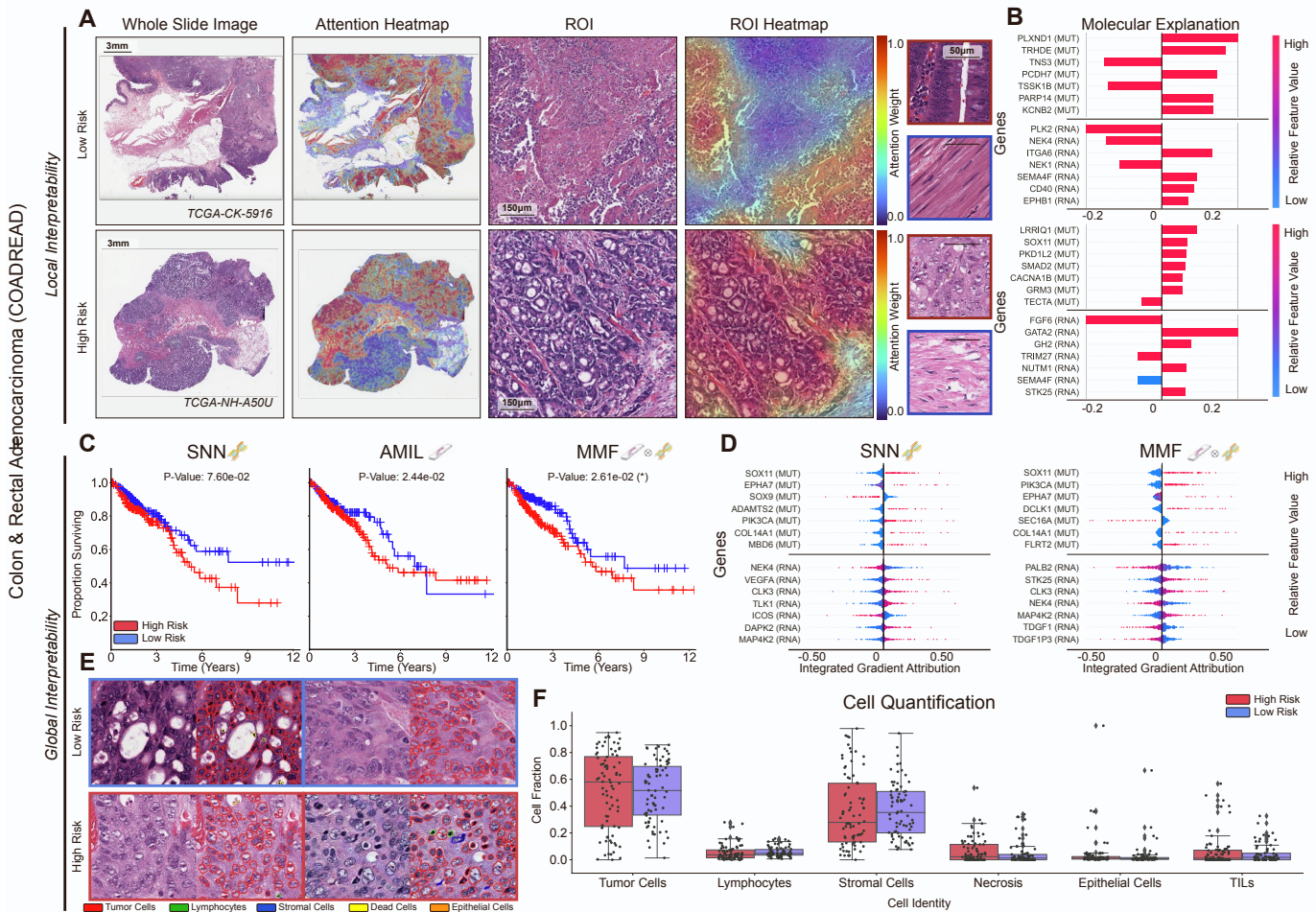


Figure S4: Quantitative performance, local model explanation, and global interpretability analyses of PORPOISE on COADREAD. Related to Figure 3, 4, 5, and 6. **A.** WSIs, associated attention heatmaps, ROIs, ROI heatmaps, and selected high attention patches from example low-risk (top) and high-risk (bottom) cases. In COADREAD ($n=338$), high attention for low-risk cases ($n=74$) tends to focus on muscularis, solid tumor growth and small nests of tumor cells, while in high-risk cases ($n=80$), high attention focuses on tumor cells invading the submucosa into the muscularis. **B.** Local gene attributions for the corresponding low-risk (top) and high-risk (bottom) cases. **C.** Kaplan–Meier curves for omics-only (left, "SNN"), histology-only (center, "AMIL") and multimodal fusion (right, "MMF"), showing improved patient stratification over AMIL and long-surviving patients in SNN. Logrank test was used to test for statistical significance in survival distributions between low- and high-risk patients (with * marked if $P\text{-Value} < 0.05$). **D.** Global gene attributions across patient cohorts according to unimodal interpretability (left, "SNN"), and multimodal interpretability (right, "MMF"). **E.** High attention patches from low-risk (top) and high-risk (bottom) cases with corresponding cell labels. **F.** Quantification of cell types in high attention patches for each disease overall, showing similar admixtures of tumor cells, lymphocytes, and stromal cells across both risk groups. Boxes indicate quartile values and whiskers extend to data points within $1.5 \times$ the interquartile range.

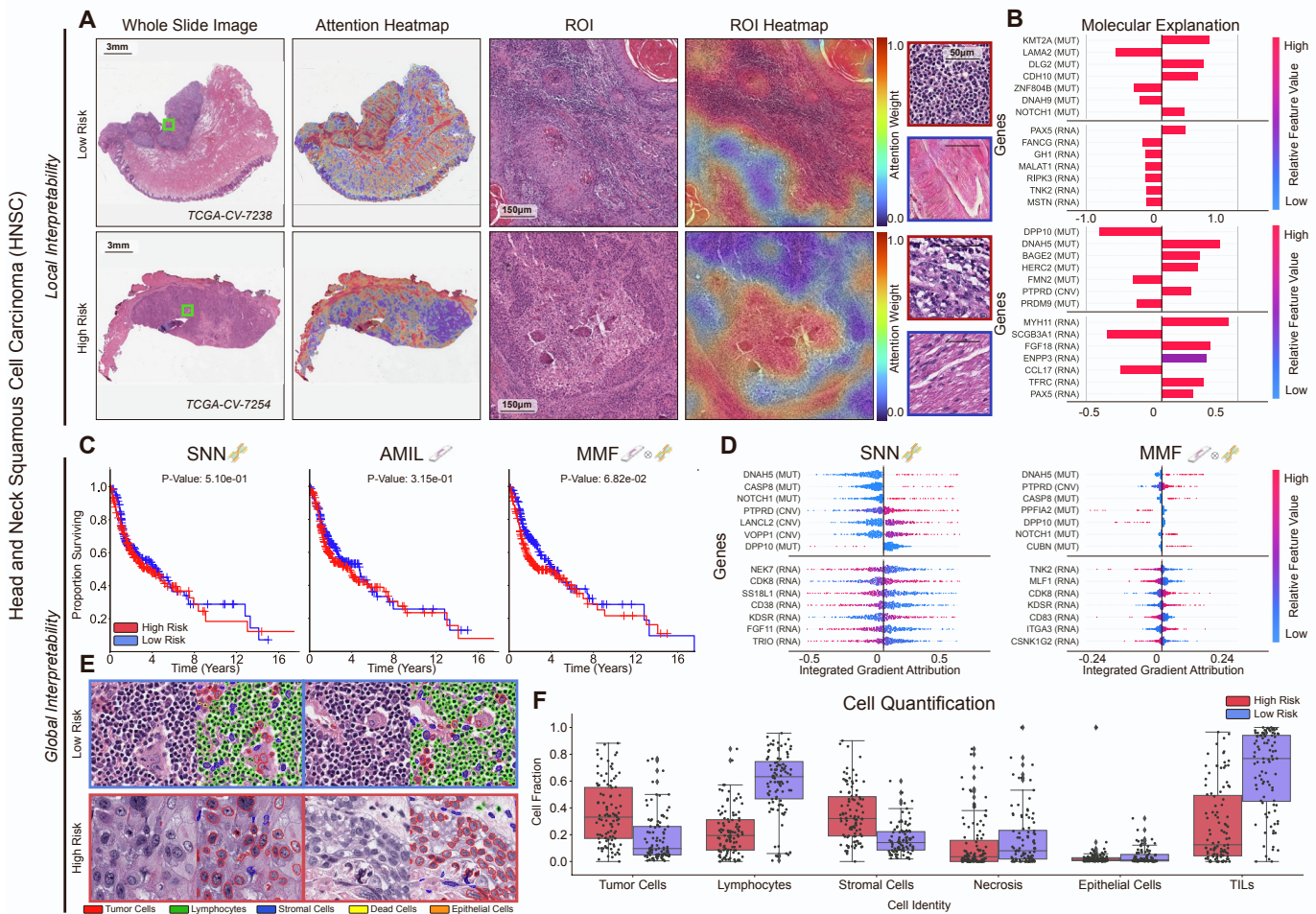


Figure S5: Quantitative performance, local model explanation, and global interpretability pooled analyses of PORPOISE on HNSC. Related to Figure 3, 4, 5, and 6. **A.** WSIs, associated attention heatmaps, ROIs, ROI heatmaps, and selected high attention patches from example low-risk (top) and high-risk (bottom) cases. In HNSC ($n=413$), high attention for low-risk cases ($n=96$) tends to focus on regions with increased tumor infiltrating lymphocytes, while in high-risk cases ($n=103$), high attention areas corresponded with regions with central necrosis. For both high and low-risk cases, the low attention regions focused on mainly background stroma. **B.** Local gene attributions for the corresponding low-risk (top) and high-risk (bottom) cases. **C.** Kaplan–Meier curves for omics-only (left, "SNN"), histology-only (center, "AMIL") and multimodal fusion (right, "MMF"), with statistically significant patient stratification between low- and high-risk groups across all models. Logrank test was used to test for statistical significance in survival distributions between low- and high-risk patients (with * marked if $P\text{-Value} < 0.05$). **D.** Global gene attributions across patient cohorts according to unimodal interpretability (left, "SNN"), and multimodal interpretability (right, "MMF"). **E.** High attention patches from low-risk (top) and high-risk (bottom) cases with corresponding cell labels. **F.** Quantification of cell types in high attention patches for each disease overall, showing increased tumor cell presence in the high-risk group, with increased lymphocyte and TIL presence in the low-risk group. Boxes indicate quartile values and whiskers extend to data points within $1.5 \times$ the interquartile range.

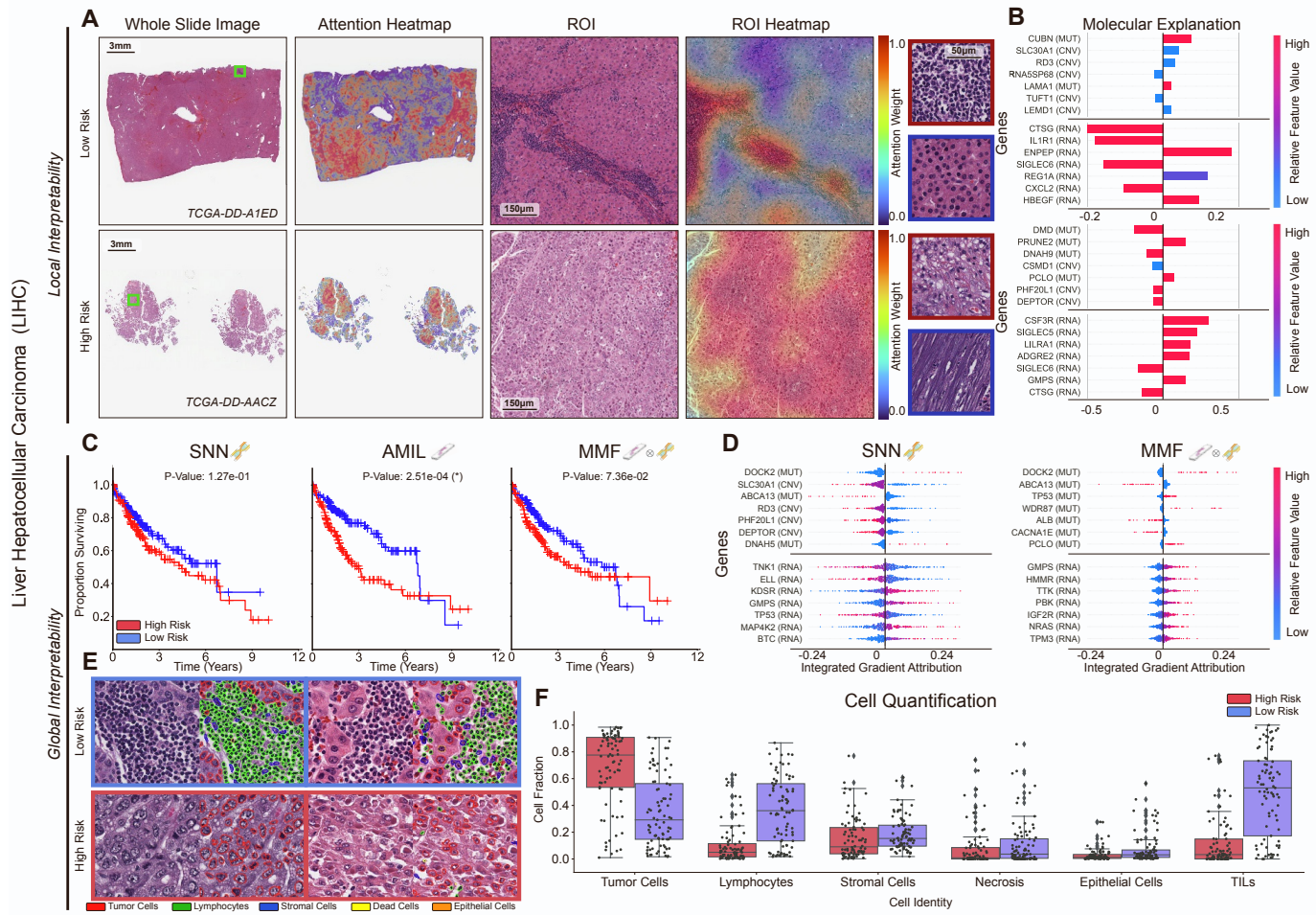


Figure S6: Quantitative performance, local model explanation, and global interpretability pooled analyses of PORPOISE on LIHC. Related to Figure 3, 4, 5, and 6. **A.** WSIs, associated attention heatmaps, ROIs, ROI heatmaps, and selected high attention patches from example low-risk (top) and high-risk (bottom) cases. In LIHC (n=332), high attention for low-risk cases (n=85) tends to focus on dense regions of lymphocytes, while in high-risk cases (n=84), high attention focuses on areas with high tumor-grade morphology, such as increased nuclear pleomorphism. **B.** Local gene attributions for the corresponding low-risk (top) and high-risk (bottom) cases. **C.** Kaplan–Meier curves for omics-only (left, "SNN"), histology-only (center, "AMIL") and multimodal fusion (right, "MMF"), showing poor stratification with SNN and better stratification in AMIL and MMF. Logrank test was used to test for statistical significance in survival distributions between low- and high-risk patients (with * marked if P-Value < 0.05). **D.** Global gene attributions across patient cohorts according to unimodal interpretability (left, "SNN"), and multimodal interpretability (right, "MMF"). **E.** High attention patches from low-risk (top) and high-risk (bottom) cases with corresponding cell labels. **F.** Quantification of cell types in high attention patches for each disease overall, showing increased tumor cell presence in high-risk patients and increased lymphocyte and TIL presence in low-risk patients. Boxes indicate quartile values and whiskers extend to data points within 1.5× the interquartile range.

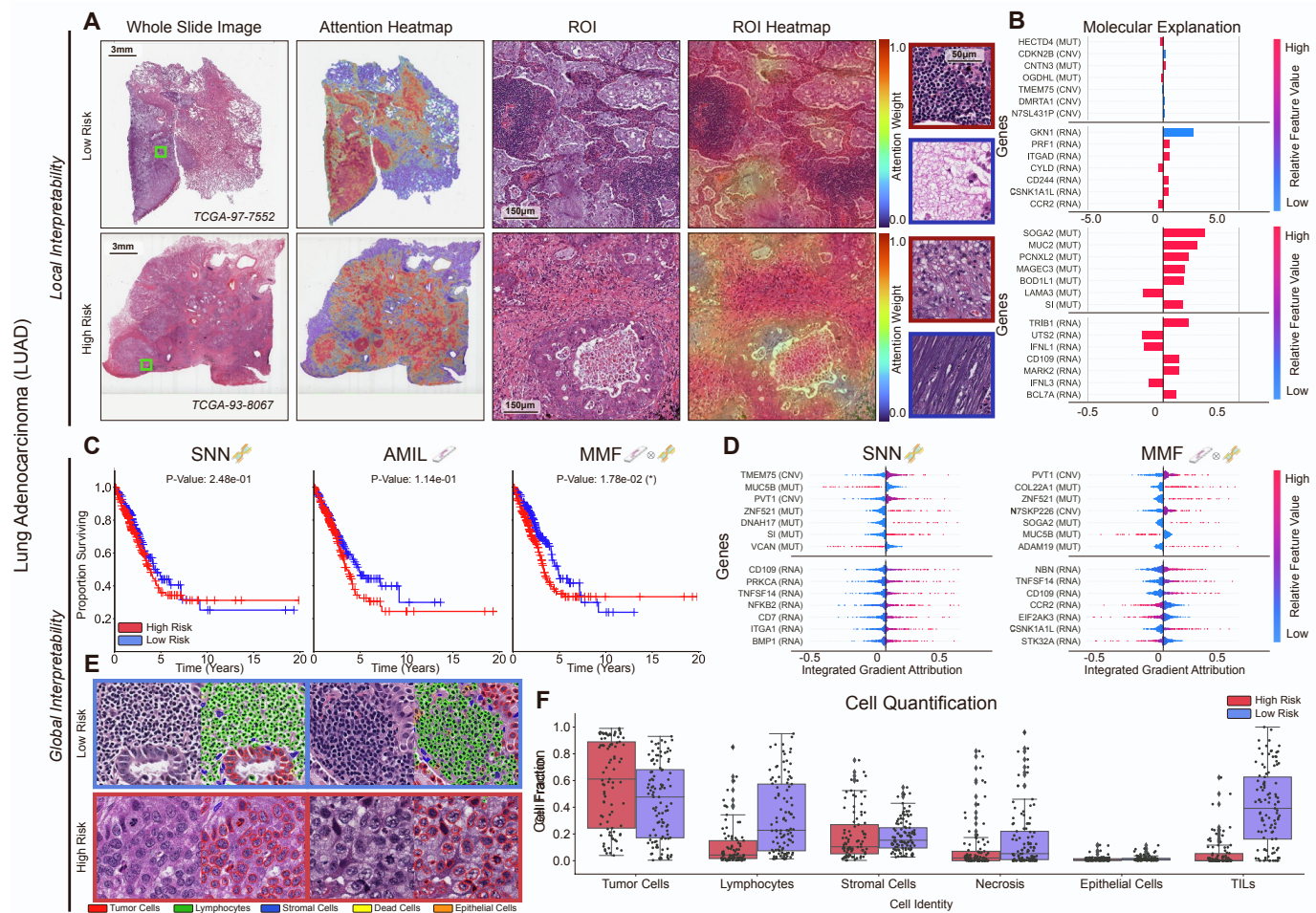


Fig. S7: Quantitative performance, local model explanation, and global interpretability analyses of PORPOISE on LUAD. Related to Figure 3, 4, 5, and 6. **A.** WSIs, associated attention heatmaps, ROIs, ROI heatmaps, and selected high attention patches from example low-risk (top) and high-risk (bottom) cases. In LUAD (n=431), high attention for low-risk cases (n=105) tends to focus on regions with dense inflammatory infiltrate, predominantly comprised of lymphocytes, and regions of mucin deposition, while in high-risk cases (n=89), high attention focuses on tumor cells with increased nuclear pleomorphism, areas of necrosis, and tumor-associated dense fibrous stroma. **B.** Local gene attributions for the corresponding low-risk (top) and high-risk (bottom) cases. **C.** Kaplan–Meier curves for omics-only (left, "SNN"), histology-only (center, "AMIL") and multimodal fusion (right, "MMF"), showing poor stratification with SNN and better stratification in AMIL and MMF. Logrank test was used to test for statistical significance in survival distributions between low- and high-risk patients (with * marked if P-Value < 0.05). **D.** Global gene attributions across patient cohorts according to unimodal interpretability (left, "SNN"), and multimodal interpretability (right, "MMF"). **E.** High attention patches from low-risk (top) and high-risk (bottom) cases with corresponding cell labels. **F.** Quantification of cell types in high attention patches for each disease overall, showing increased lymphocyte and TIL presence in low-risk patients. Boxes indicate quartile values and whiskers extend to data points within 1.5× the interquartile range.

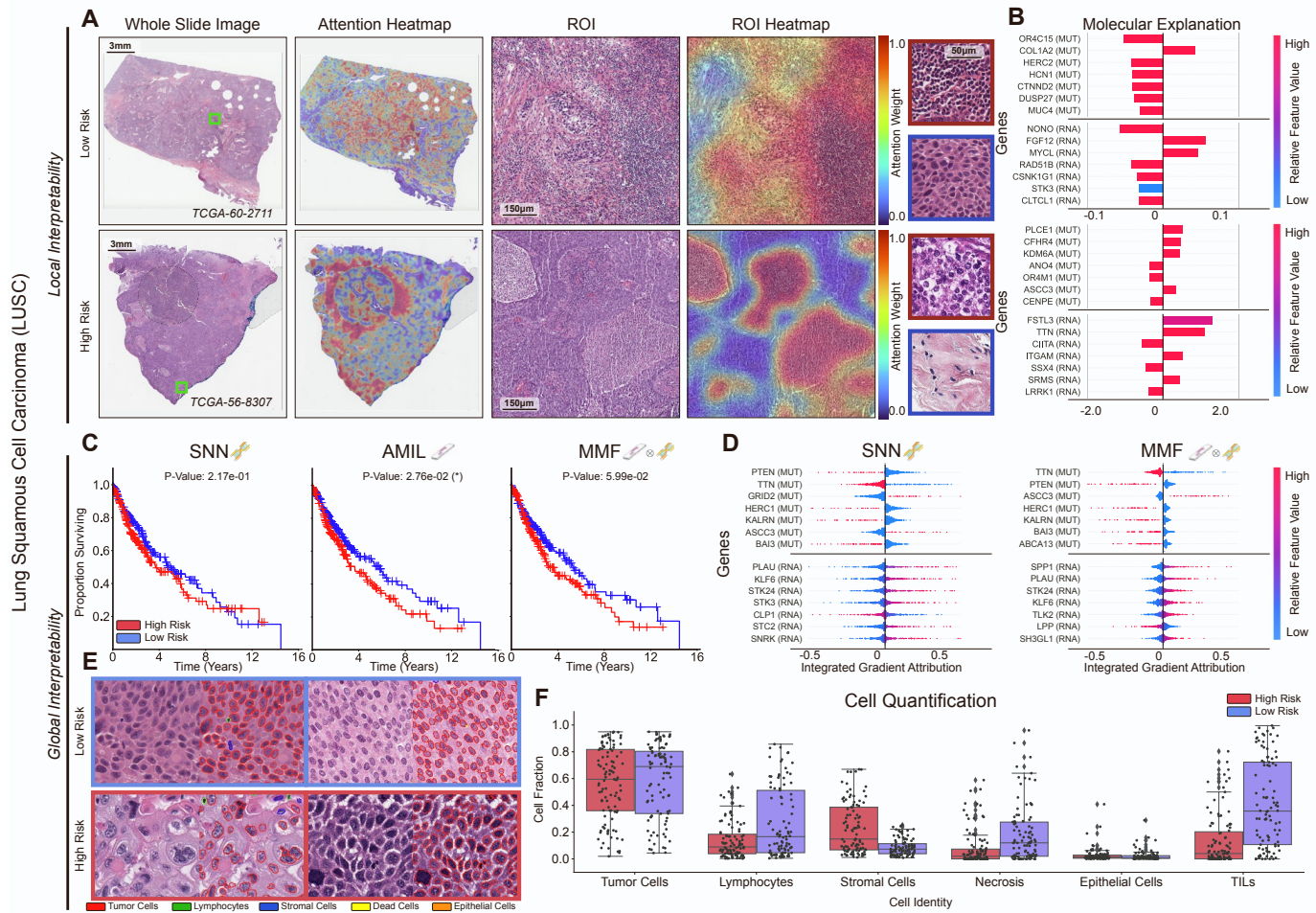


Figure S8: Quantitative performance, local model explanation, and global interpretability pooled analyses of PORPOISE on LUSC. Related to Figure 3, 4, 5, and 6. **A.** WSIs, associated attention heatmaps, ROIs, ROI heatmaps, and selected high attention patches from example low-risk (top) and high-risk (bottom) cases. In LUSC (n=441), high attention for low-risk cases (n=97) tends to focus on regions with dense inflammatory infiltrate, predominantly comprised of lymphocytes (presumed TILs), while in high-risk cases (n=103), high attention focuses on regions of central necrosis within tumor nests. **B.** Local gene attributions for the corresponding low-risk (top) and high-risk (bottom) cases. **C.** Kaplan–Meier curves for omics-only (left, "SNN"), histology-only (center, "AMIL") and multimodal fusion (right, "MMF"), showing improved patient stratification over AMIL and late-stage patients in SNN. Logrank test was used to test for statistical significance in survival distributions between low- and high-risk patients (with * marked if P-Value < 0.05). **D.** Global gene attributions across patient cohorts according to unimodal interpretability (left, "SNN"), and multimodal interpretability (right, "MMF"). **E.** High attention patches from low-risk (top) and high-risk (bottom) cases with corresponding cell labels. **F.** Quantification of cell types in high attention patches for each disease overall, showing increased lymphocyte and TIL presence in low-risk patients. Boxes indicate quartile values and whiskers extend to data points within 1.5× the interquartile range.

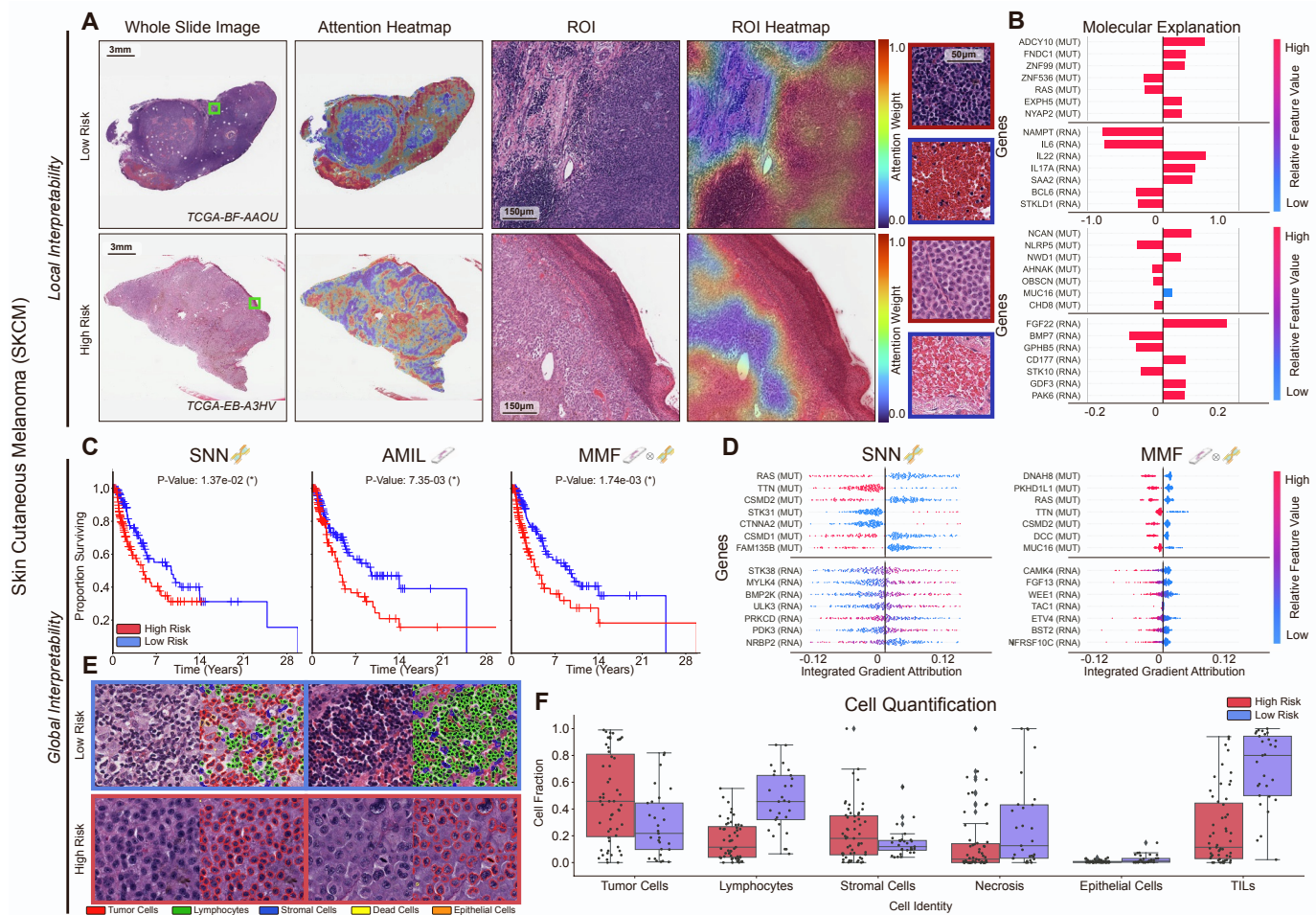


Figure S9: Quantitative performance, local model explanation, and global interpretability pooled analyses of PORPOISE on SKCM. Related to Figure 3, 4, 5, and 6. **A.** WSIs, associated attention heatmaps, ROIs, ROI heatmaps, and selected high attention patches from example low-risk (top) and high-risk (bottom) cases. In SKCM (n=222), high attention regions for low-risk cases (n=29) focused on tumor-infiltrating lymphocytes, while the high attention regions for high-risk cases (n=55) paid more attention to ulcerated regions and regions of densely packed tumor cells. For both high and low-risk cases, the low attention regions focused mainly on background blood. **B.** Local gene attributions for the corresponding low-risk (top) and high-risk (bottom) cases. **C.** Kaplan–Meier curves for omics-only (left, "SNN"), histology-only (center, "AMIL") and multimodal fusion (right, "MMF"), showing better patient stratification in AMIL and SNN. Logrank test was used to test for statistical significance in survival distributions between low- and high-risk patients (with * marked if P-Value < 0.05). **D.** Global gene attributions across patient cohorts according to unimodal interpretability (left, "SNN"), and multimodal interpretability (right, "MMF"). **E.** High attention patches from low-risk (top) and high-risk (bottom) cases with corresponding cell labels. **F.** Quantification of cell types in high attention patches for each disease overall, showing increased tumor cell and necrosis presence in the high-risk group, with increased lymphocyte and TIL presence in the low-risk group. Boxes indicate quartile values and whiskers extend to data points within 1.5× the interquartile range.

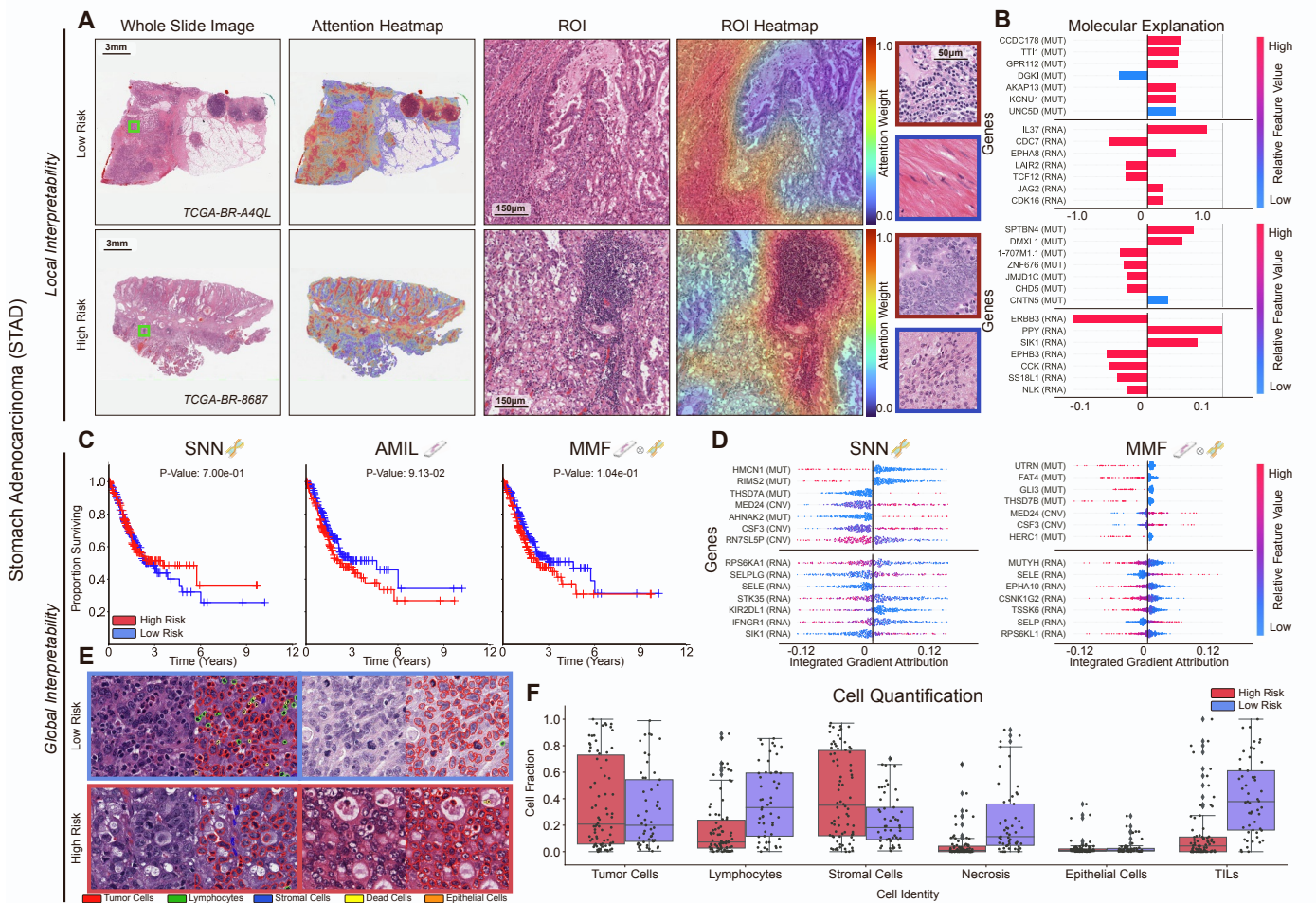


Figure S10: Quantitative performance, local model explanation, and global interpretability pooled analyses of PORPOISE on STAD. Related to Figure 3, 4, 5, and 6.

A. WSIs, associated attention heatmaps, ROIs, ROI heatmaps, and selected high attention patches from example low-risk (top) and high-risk (bottom) cases. In STAD ($n=347$), high attention for low-risk cases ($n=53$) tends to focus on dense regions of tumor, lymphocytes, and muscularis, while in high-risk cases ($n=78$), high attention focuses on dense regions of tumor and lymphocytes.

B. Local gene attributions for the corresponding low-risk (top) and high-risk (bottom) cases.

C. Kaplan–Meier curves for omics-only (left, "SNN"), histology-only (center, "AMIL") and multimodal fusion (right, "MMF"), showing better patient stratification in AMIL and SNN. Logrank test was used to test for statistical significance in survival distributions between low- and high-risk patients (with * marked if $P\text{-Value} < 0.05$).

D. Global gene attributions across patient cohorts according to unimodal interpretability (left, "SNN"), and multimodal interpretability (right, "MMF").

E. High attention patches from low-risk (top) and high-risk (bottom) cases with corresponding cell labels.

F. Quantification of cell types in high attention patches for each disease overall, showing increased lymphocyte and TIL presence in the low-risk group. Boxes indicate quartile values and whiskers extend to data points within $1.5 \times$ the interquartile range.

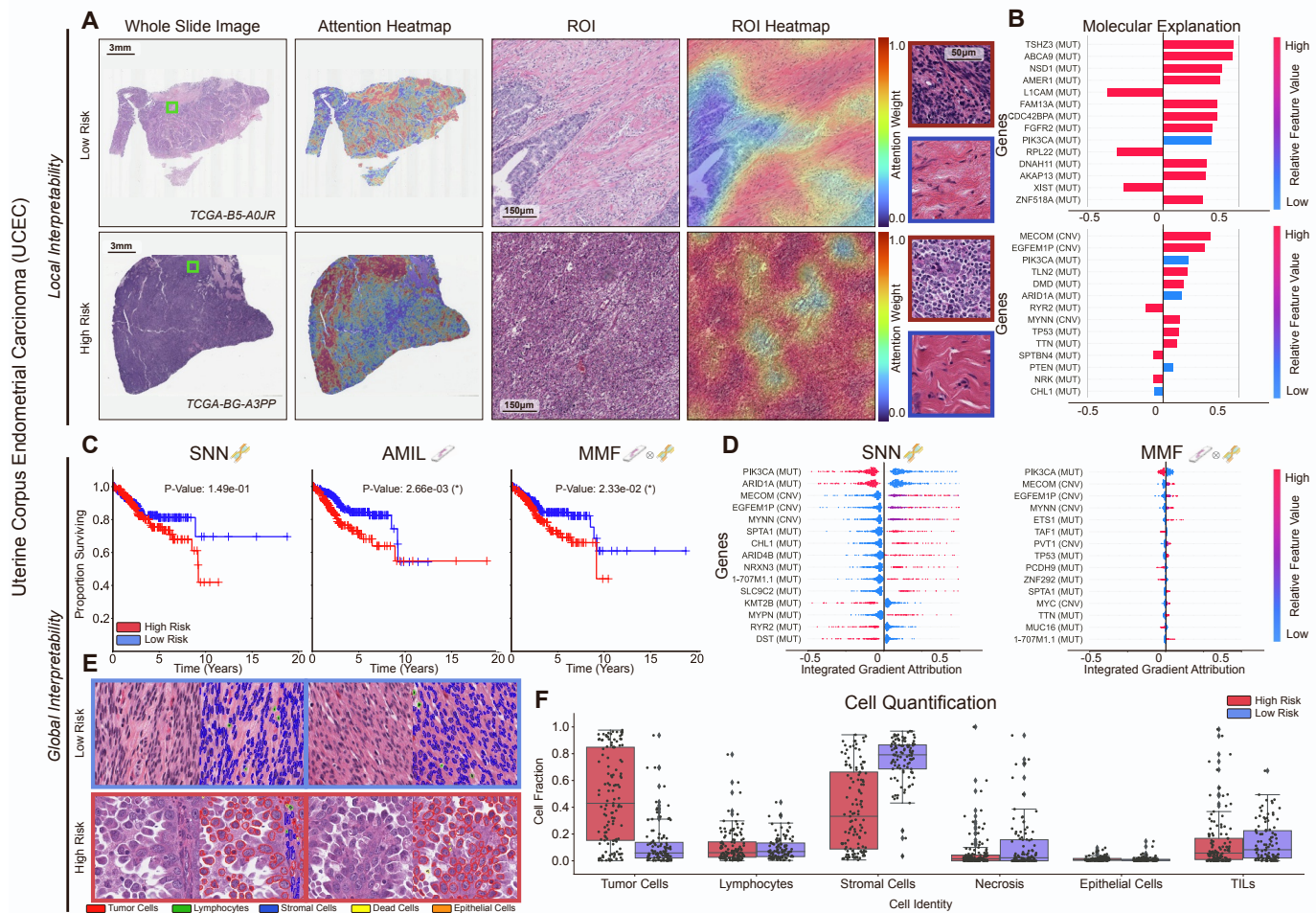


Figure S11: Quantitative performance, local model explanation, and global interpretability pooled analyses of PORPOISE on UCEC. Related to Figure 3, 4, 5, and 6. **A.** WSIs, associated attention heatmaps, ROIs, ROI heatmaps, and selected high attention patches from example low-risk (top) and high-risk (bottom) cases. In UCEC ($n=460$), high attention for low-risk cases ($n=104$) tends to focus on background myometrium, while in high-risk cases ($n=125$), high attention focuses on tumor regions, especially those with increased nuclear pleomorphism and atypia. **B.** Local gene attributions for the corresponding low-risk (top) and high-risk (bottom) cases. **C.** Kaplan–Meier curves for omics-only (left, "SNN"), histology-only (center, "AMIL") and multimodal fusion (right, "MMF"), showing improved patient stratification over AMIL and late-stage patients in SNN. Logrank test was used to test for statistical significance in survival distributions between low- and high-risk patients (with * marked if $P\text{-Value} < 0.05$). **D.** Global gene attributions across patient cohorts according to unimodal interpretability (left, "SNN"), and multimodal interpretability (right, "MMF"). **E.** High attention patches from low-risk (top) and high-risk (bottom) cases with corresponding cell labels. **F.** Quantification of cell types in high attention patches for each disease overall, showing increased tumor cell presence in high-risk patients and increased stromal cell presence in low-risk patients. Boxes indicate quartile values and whiskers extend to data points within $1.5 \times$ the interquartile range.

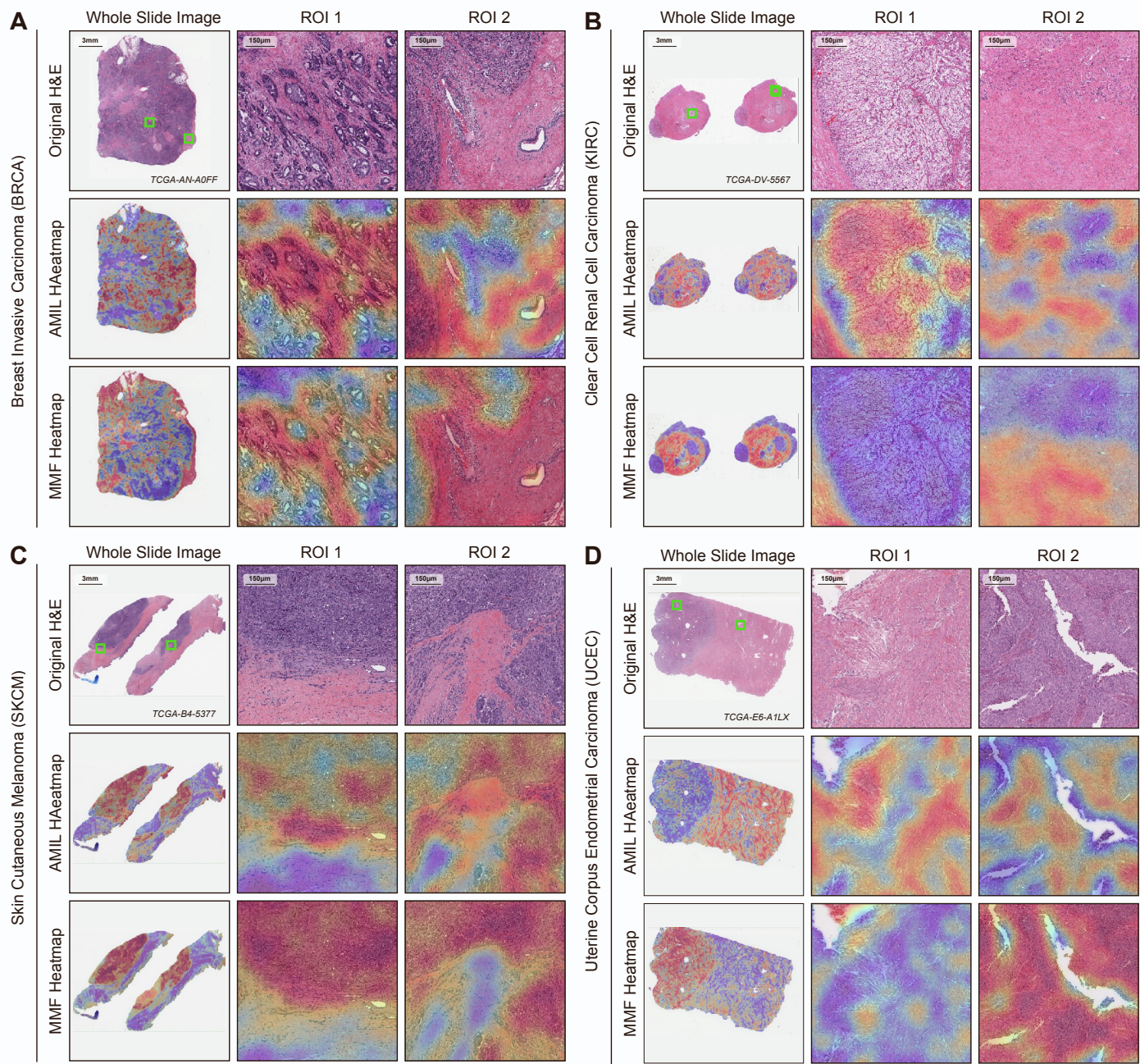


Figure S12: Exemplars of attention shift from unimodal to multimodal interpretability in WSIs. Related to Figure 3, S3, S9, and S11. Using PORPOISE, we investigated and examined how feature importance in high attention regions shifts when comparing AMIL (trained with histology-only) vs. MMF (histology conditioned with molecular profiles). In the assessment of each cancer type, "ROI 1" corresponds to a region where attention decreased from AMIL to MMF, and "ROI 2" corresponds to a region where attention increased from AMIL to MMF. **A.** In BRCA, attention shifted away from dense areas of tumor to both tumor and stromal regions in MMF. **B.** In KIRC, both stroma and tumor regions with classic "chicken-wire" vasculature are present in high attention regions in AMIL, whereas MMF attends to only stroma and completely segments out the tumor regions. **C.** In SKCM, both AMIL and MMF were able to localize tumor regions, with MMF being able to identify clear tumor-stroma boundaries. **D.** In UCEC, attention shifted towards dense tumor regions and away from stroma in MMF.

Supplemental Tables

Table S1. TCGA Pan-Cancer Demographic Characteristics. Related to Figure 1 and 2.

Cancer	No. Cases	Age	Gender M/F	White/Black/Other/NA	Grade 1/2/3/4/NA	Censorship
BLCA	373	68.0 ± 10.6	277/96	297/20/42/0/14	20/0/0/351/2	0.547
BRCA	730	57.4 ± 13.3	10/720	490/138/43/1/62	NA	0.860
COADREAD	339	64.9 ± 13.0	180/159	247/56/12/1/27	NA	0.761
HNSC	416	61.2 ± 11.9	307/109	353/42/8/2/13	53/247/100/4/12	0.526
KIRC	345	60.1 ± 12.0	219/126	283/50/7/0/6	11/146/135/46/7	0.733
KIRP	259	61.5 ± 12.1	189/70	183/58/6/1/12	NA	0.846
LGG	479	43.4 ± 13.4	268/211	453/21/7/1/10	0/229/249/0/1	0.766
LIHC	333	59.3 ± 13.2	223/110	165/13/149/0/8	44/160/112/12/5	0.655
LUAD	453	65.2 ± 10.0	208/245	344/51/7/1/52	NA	0.651
LUSC	450	67.2 ± 8.6	336/114	315/27/9/0/99	NA	0.573
PAAD	166	64.5 ± 11.0	91/75	146/6/11/0/4	26/91/45/2/2	0.458
SKCM	230	59.5 ± 15.6	140/90	220/1/9/0/6	NA	0.613
STAD	348	65.3 ± 10.5	227/121	211/10/80/1/46	8/123/209/0/8	0.601
UCEC	480	63.9 ± 11.1	0/480	326/96/19/11/29	94/113/265/8	0.844

Table S2. c-Index Model Performances on Survival Prediction across 14 Cancer Types with Logrank Test Significance for Patient Stratification. Related to Figure 2.

Study	SNN	P-Value	MIL	P-Value	MMF	P-Value
BLCA	0.595 (0.535-0.637)	2.35e-03	0.542 (0.486-0.580)	2.14e-01	0.631 (0.572-0.671)	2.30e-03
BRCA	0.586 (0.525-0.643)	2.19e-01	0.560 (0.489-0.615)	2.70e-01	0.628 (0.571-0.680)	3.99e-03
COADREAD	0.580 (0.496-0.654)	7.60e-02	0.546 (0.466-0.617)	2.44e-01	0.640 (0.562-0.705)	2.61e-02
HNSC	0.516 (0.478-0.572)	5.10e-01	0.564 (0.507-0.592)	3.15e-01	0.573 (0.525-0.617)	6.82e-02
KIRC	0.633 (0.567-0.697)	2.99e-02	0.567 (0.508-0.650)	5.98e-02	0.659 (0.589-0.709)	4.38e-06
KIRP	0.779 (0.678-0.857)	2.27e-03	0.539 (0.408-0.625)	5.86e-01	0.816 (0.705-0.880)	3.83e-04
LGG	0.792 (0.738-0.841)	5.68e-10	0.668 (0.614-0.734)	1.82e-04	0.808 (0.745-0.844)	7.09e-12
LIHC	0.594 (0.534-0.656)	1.27e-01	0.618 (0.563-0.684)	2.51e-04	0.622 (0.559-0.681)	7.36e-02
LUAD	0.554 (0.493-0.613)	2.48e-01	0.548 (0.489-0.597)	1.14e-01	0.600 (0.548-0.657)	1.78e-02
LUSC	0.522 (0.476-0.572)	2.17e-01	0.561 (0.500-0.597)	2.76e-02	0.538 (0.472-0.575)	5.99e-02
PAAD	0.593 (0.507-0.656)	5.59e-02	0.580 (0.485-0.613)	2.30e-01	0.653 (0.571-0.696)	1.69e-03
SKCM	0.644 (0.568-0.691)	1.37e-02	0.607 (0.509-0.661)	7.35e-03	0.651 (0.581-0.710)	1.74e-03
STAD	0.513 (0.453-0.560)	7.00e-01	0.556 (0.494-0.598)	9.13e-02	0.563 (0.496-0.607)	1.04e-01
UCEC	0.580 (0.484-0.621)	1.49e-01	0.638 (0.563-0.701)	2.66e-03	0.634 (0.527-0.667)	2.33e-02
Overall	0.606	-	0.578	-	0.644	-